J. Fluid Mech. (2021), *vol*. 929, A34, doi:10.1017/jfm.2021.884

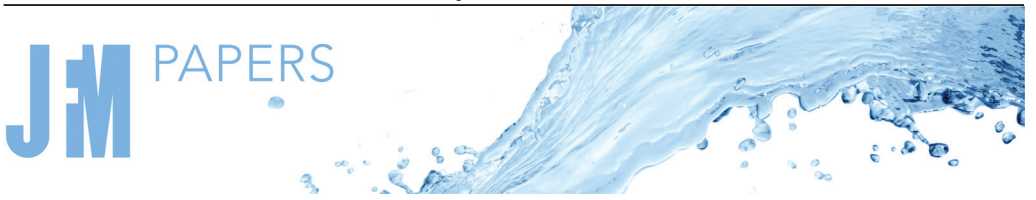

Mechanism of reduction of aeroacoustic sound by porous material: comparative study of microscopic and macroscopic models

Yasunori Sato[1,2] **and Yuji Hattori**[1,†]

[1]Institute of Fluid Science, Tohoku University, Sendai 980-8577, Japan

[2]Graduate School of Information Sciences, Tohoku University, Sendai 980-8579, Japan

(Received 4 February 2021; revised 7 September 2021; accepted 5 October 2021)

The effects of porous material on the aeroacoustic sound generated in a two-dimensional low-Reynolds-number flow ($Re = 150$) past a circular cylinder are studied by direct numerical simulation in which the acoustic waves of small amplitudes are obtained directly as a solution to the compressible Navier–Stokes equations. Two models are introduced for the porous material: the microscopic model, in which the porous material is a collection of small cylinders, and the macroscopic model, in which the porous material is continuum characterized by permeability. The corrected volume penalization method is used to deal with the core cylinder, the small cylinders and the porous material. In the microscopic model, significant reduction of the aeroacoustic sound is found depending on the parameters; the maximum reduction of 24.4 dB from the case of a bare cylinder is obtained. The results obtained for the modified macroscopic model are in good agreement with those obtained for the microscopic model converted by the theory of homogenization, which establishes that the microscopic and macroscopic models are consistent and valid. The detailed mechanism of sound reduction is elucidated. The presence of a fluid region between the porous material and the core cylinder is important for sound reduction. When the sound is strongly reduced, the pressure field behind the cylinder becomes nearly uniform with a high value to stabilize the shear layer in the wake; as a result, the vortex shedding behind the cylinder is delayed to the far wake to suppress the unsteady vortex motion near the cylinder, which is responsible for the aeroacoustic sound.

Key words: aeroacoustics, noise control, porous media

† Email address for correspondence: hattori@ifs.tohoku.ac.jp

1. Introduction

Noise reduction is one of the most important problems for various engineering devices. For example, the maximum speeds of high-speed trains in Japan are often limited by the allowable sound pressure level of noise radiated from them so as not to disturb residents near the railroads. The noise is usually dominated by aeroacoustic noise, whose power P increases rapidly with the characteristic speed U of the device as $P \propto U^{5\sim8}$. Many efforts have been devoted to reduce aeroacoustic noise by e.g. changing the shapes of devices and removing roughness. However, some parts such as pantographs of trains cannot be removed, which necessitates the need of other methods for noise reduction.

Porous materials have been shown to be effective and promising for noise reduction. Sueki *et al.* (2010) applied a porous material to reduce the aeroacoustic noise generated in the flow past a circular cylinder. Their experiment showed that the noise is significantly reduced when a solid cylinder is covered by the porous material. The mechanism of reduction is that the porous material hinders the momentum of the wake and suppresses the unsteady motion of vortices in the wake (see also Naito & Fukagata 2012). Nishimura & Goto (2010) studied the effects of pile fabrics on the aeroacoustic noise generated in the flow past a circular cylinder by experiments. A similar problem was studied numerically by Xu, Zheng & Wilson (2010). Liu *et al.* (2015) considered the aerodynamic sound from tandem cylinders covered by a porous material by numerical simulation. See also the works of Geyer, Sarradj & Fritzsche (2010), Herr *et al.* (2014), Delfs *et al.* (2014), Giret & Sengissen (2015) and Geyer & Sarradj (2016). Although the above works showed that a porous material is effective for noise reduction, such materials are not widely used in reality. This is partly because the detailed mechanism of sound reduction has not been fully elucidated; in other words, the aeroacoustic sound can be further reduced by clarifying in more detail the effects of the porous material on the unsteady vortex motion near the objects, which generates the aeroacoustic sound. Moreover, the lack of reliable and convenient tools for evaluating sound in flows which involve a porous material is another reason; experiments are not convenient because it is not easy to change the parameters and properties of the porous material and the results are often limited; most of the numerical works so far rely on aeroacoustic analogies, and the disadvantages of these will be discussed later in this section.

In this paper, we study the effects of a porous material on the reduction of aeroacoustic sound by direct numerical simulation (DNS); here DNS implies that the sound pressure is directly obtained by solving the compressible Navier–Stokes equations without using acoustic analogies or solving additional equations such as a linear wave equation. Our main objectives are to clarify the detailed mechanism of sound reduction and to reveal what are essential for sound reduction. Two models of the porous material are considered: a microscopic model, in which the porous material is a collection of small cylinders, and a macroscopic model, in which the porous material is a continuum characterized by permeability. We will show that the results obtained by the two models are in good agreement, which establishes that the models are reliable tools for investigating the aeroacoustic sound in flows which involve a porous material; they are also convenient becaue it is easy to change the geometry and properties of the porous material. For example, they can be used to optimize the porous material for noise reduction.

DNS has been established as an effective tool of computational aeroacoustics supported by the rapid development of computational resources (Colonius & Lele 2004; Wang, Freund & Lele 2006); it has been used to study aeroacoustic sound not only in laminar flows (Mitchell, Lele & Moin 1995; Inoue & Hattori 1999; Inoue, Hattori & Sasaki 2000;

Hattori & Llewellyn Smith 2002; Gloerfelt, Bailly & Juvé 2003; Barré, Bogey & Bailly 2008; Müller 2008; Nakashima 2008; Hattori & Komatsu 2017) but also in turbulent flows (Mitchell, Lele & Moin 1999; Freund, Lele & Moin 2000). DNS of aeroacoustic sound has advantages over the hybrid method frequently used in computational aeroacoustics. In the hybrid method, the sound sources are obtained numerically by solving the incompressible Navier–Stokes equations assuming low-Mach-number flow and the sound pressure is calculated using aeroacoustic analogies. The accuracy of the sound should be carefully addressed because several assumptions including low-Mach-number flow and compactness of the objects are used in most of the aeroacoustic analogies. More importantly, feedback from sound or a compressible component on the flow is missing in the hybrid method. In contrast, DNS requires no assumptions and contains all physics.

We also point out that problems which deal with aeroacoustic sound and the porous material simultaneously have not been studied by DNS. In the numerical simulation by Xu *et al.* (2010), the flow is assumed incompressible and pressure fluctuations in the near field, which are different from the sound pressure, are used as a measure of sound pressure; Liu *et al.* (2015) converted the results obtained by RANS simulation to sound using the acoustic analogy by Ffowcs Williams & Hawkings (1969). There have been many numerical works on incompressible flows involving a porous material. Most of them use macroscopic models of the porous material such as Darcy's law and Brinkman's equation. Microscopic models are mostly used to derive macroscopic properties such as permeability (Perrot, Chevillotte & Panneton 2007; Hwang & Advani 2010; Lopez Penha *et al.* 2011; Matsumura & Jackson 2014; Breugem, van Dijk & Delfos 2015; Matsumura, Jenne & Jackson 2015). For example, Perrot *et al.* (2007) calculated the dynamic viscous permeability for a two-dimensional model of a periodic open-cell aluminium foam not only numerically and but also experimentally, and showed that numerical simulation gives good prediction of the permeability. Matsumura & Jackson (2014) studied a two-dimensional flow through periodic packs of polydisperse cylinders by an immersed boundary method; they showed that the normalized permeability is a function of porosity and polydiversity. To the best of the authors' knowledge, however, numerical studies of microscopic models for compressible flows have been limited to computational homogenization in the linear acoustic regime in the absence of nonlinear flows (Gao *et al.* 2016). It is not evident that the macroscopic models can be used to simulate compressible flows in which both flows and acoustic waves are affected by the porous material, although there are some results supporting that Darcy's law is valid for propagation of linear acoustic waves in the low-frequency approximations (Fellah & Depollier 2000); the present study will provide a positive answer to this problem.

This paper is organized as follows. In § 2, the problem formulation and the numerical methods are presented; the microscopic and macroscopic models are also introduced. In § 3, the results obtained for the microscopic model are presented, while those obtained for the macroscopic model are presented in § 4. In § 5, the relation between the microscopic and macroscopic model is discussed by introducing a modified macroscopic model. The detailed mechanism of sound reduction is discussed in § 6. We provide our conclusions in § 7.

2. Problem formulation and numerical methods

2.1. *Problem formulation and models*

We consider a compressible flow past a circular cylinder covered by porous material (figure 1). The circular cylinder is referred to as the core cylinder below. The diameter

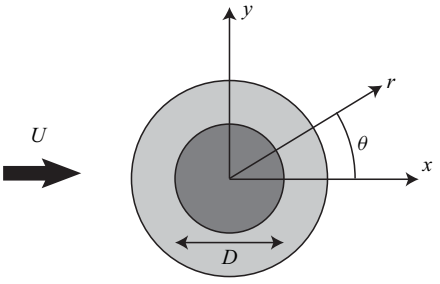

Figure 1. Schematic diagram of flow model. The dark grey region and the light grey region correspond to the core cylinder (rigid body) and the porous material, respectively.

of the core cylinder is denoted by D, while the velocity of the incoming uniform flow is denoted by U. The porous material occupies the annulus $0.5D \leq r \leq D_o/2 = 0.9D$ with thickness $h = 0.9D - 0.5D = 0.4D$ as in the experiments by Sueki *et al.* (2010), although the thickness is changed in § 4 to investigate the effects of the thickness of the porous material. This value of the thickness may look too large because the drag would increase which is not desirable; however, this is not the case in applications to high-speed trains in which increase in the drag of pantographs has negligible effects on the total drag of the trains and the reduction of the aeroacoustic noise is the most important issue. The flow is assumed two-dimensional (2-D). The Mach number of the incoming flow and the Reynolds number based on the core cylinder are fixed to $M_\infty = U/c_\infty = 0.2$ and $Re = \rho_\infty UD/\mu = 150$, respectively, where c_∞ and ρ_∞ are the speed of sound and density at infinity, respectively, and μ is the viscosity which is assumed constant. This 2-D low-Reynolds-number flow is chosen because it is a canonical flow frequently studied as a benchmark problem (Inoue & Hatakeyama 2002; Müller 2008; Tsutahara *et al.* 2008). The fluid is assumed to be an ideal gas.

We introduce two models for the porous material: a microscopic model and a macroscopic model (figure 2). In the microscopic model, the porous material is a collection of small cylinders whose diameter is $d_s = 0.03D$; N_θ small cylinders are placed at regular intervals in the azimuthal direction on the circle $r = r_i (i = 1, \ldots, N_r)$, which implies that the total number of the small cylinders is $N_r N_\theta$. The radius r_i is set to

$$r_i = (0.9D - 0.5d_s) - \frac{i-1}{N_r} h, \tag{2.1}$$

so that the outermost cylinders are included in the porous material and touch its boundary and the innermost cylinders do not touch the core cylinder. The azimuthal positions of the small cylinders on the adjacent circles differ by π/N_θ to form a staggered formation (figure 2*a*). The diameter of the small cylinders is set to the smallest value which can be resolved by the present numerical method and the available computational resources.

In the macroscopic model, however, the porous material is a continuous region characterized by permeability (figure 2*b*).

2.2. *Numerical methods*

We used the corrected volume penalization method (Komatsu, Iwakami & Hattori 2016), which is one of the immersed boundary methods of continuous type and has been shown to correctly resolve the aeroacoustic sound of small amplitude in complex and/or time-varying geometry (Komatsu *et al.* 2016; Hattori & Komatsu 2017;

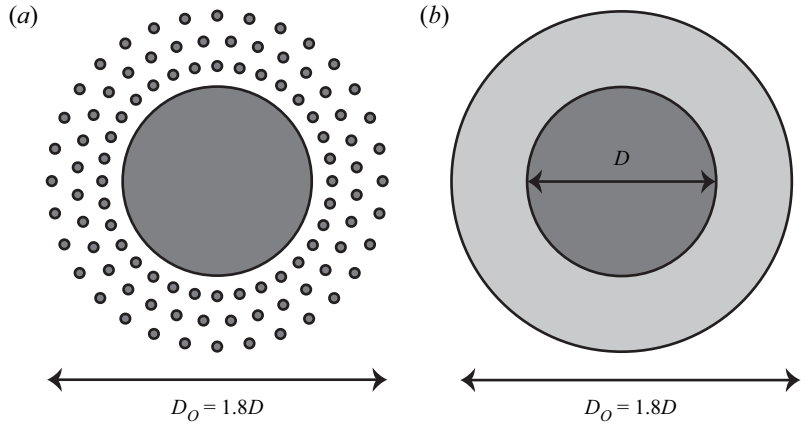

Figure 2. (*a*) Microscopic model (with $N_r = 3$ and $N_\theta = 32$) and (*b*) macroscopic model.

Iwagami *et al.* 2021). In this method, the compressible Navier–Stokes equations in the primitive variables $(\rho, \boldsymbol{u}, p)$, where ρ is the density of the fluid, u_i is the velocity and p is the pressure, are supplemented with penalization terms as

$$\frac{\partial \rho}{\partial t} + \frac{\partial}{\partial x_j}(\rho u_j) = -\left(\frac{1}{\phi_n} - 1\right)\chi \frac{\partial}{\partial x_j}[\rho(u_j - U_{0,j})], \tag{2.2}$$

$$\rho\left(\frac{\partial u_i}{\partial t} + u_j \frac{\partial u_i}{\partial x_j}\right) = -\frac{\partial p}{\partial x_i} + \frac{\partial \tau_{ij}}{\partial x_j} - \frac{\chi}{\eta}(u_i - U_{0,i}), \tag{2.3}$$

$$\frac{\partial p}{\partial t} + u_j \frac{\partial p}{\partial x_j} + \gamma p \frac{\partial u_j}{\partial x_j} = (\gamma - 1)\left[\kappa \frac{\partial^2 T}{\partial x_j \partial x_j} + \tau_{ij}\frac{\partial u_i}{\partial x_j} - \frac{\chi}{\eta_T}(T - T_0)\right], \tag{2.4}$$

where $\tau_{ij} = \mu(\partial u_i/\partial x_j + \partial u_j/\partial x_i - \frac{2}{3}(\partial u_l/\partial x_l)\delta_{ij})$ is the viscous stress tensor, T is the temperature, $U_{0,i}$ and T_0 are the velocity and the temperature of the rigid bodies, respectively, η is the viscous permeability and η_T is the thermal permeability; ϕ_n is the porosity of the rigid bodies originally introduced by Liu & Vasilyev (2007) in order for the acoustic waves to reflect at the surface of the rigid bodies correctly. The terms which are proportional to χ in (2.2)–(2.4) are called penalization terms. The mask function χ is defined as

$$\chi(\boldsymbol{x}, t) = \begin{cases} 1 & \text{if } \boldsymbol{x} \in \text{ rigid bodies,} \\ 0 & \text{otherwise.} \end{cases} \tag{2.5}$$

It is pointed out that the equations in the conservation form (Komatsu *et al.* 2016) were solved numerically in the actual simulations.

The same methods as used by Komatsu *et al.* (2016) were used for spatial discretization and time marching. Namely, a finite difference method is adopted to discretize the above set of equations on a rectangular grid. Spatial derivatives are approximated by the sixth-order accurate compact scheme (Lele 1992) except for the penalization terms which are approximated by the central finite difference of fourth-order accuracy. For time marching, the second-order implicit method is used for the penalization terms, while the second-order Adams–Bashforth method is used for the other terms. The numerical domain and computational grids are also set up as was done by Komatsu *et al.* (2016). Namely, a wide domain $|x|, |y| \leq 1000D$ is decomposed into four regions of different grid spacings required to resolve the flow: the boundary layer region, the flow region, the sound

region and the buffer region. For the details, see Appendix A; also see Komatsu *et al.* (2016) and Hattori & Komatsu (2017). The minimum grid size is set to $4.75 \times 10^{-3}D$ and $9.5 \times 10^{-3}D$ in the microscopic and the macroscopic models, respectively. The convergence study performed for the microscopic model confirms that the aeroacoustic waves are resolved with sufficient accuracy (see Appendix B). The numbers of grid points are 1794×1662 and 1532×1540 in the microscopic and the macroscopic models, respectively. The non-reflecting boundary conditions (Poinsot & Lele 1992) were imposed at the far boundaries, while possible reflections at the far boundaries were removed by grid stretching and spatial filtering by the compact scheme of sixth-order accuracy (Lele 1992).

The other parameters were chosen as follows. The Prandtl number $Pr = \gamma\mu/\kappa$ was set to 0.72, where the ratio of the specific heats γ was set to 1.4. In the rigid bodies, the porosity ϕ_n was set to 0.1 and the viscous and thermal permeabilities were set to $\eta = \eta_T = 10^{-4}$ as was done by Hattori & Komatsu (2017). In the macroscopic model, the permeabilities of the porous material were changed as $10^{-3} \leq \eta = \eta_T \leq 10^{3}$, while the porosity was fixed to $\phi_n = 0.98$. This choice of porosity is discussed in Appendix C, where it is confirmed that the results were nearly unchanged when a different relation between ϕ_n and η was used. Note that the penalization term in (2.2) which involves ϕ_n is a numerical one introduced for rigid bodies; in this regard, ϕ_n is a numerical porosity rather than the actual porosity of the porous material. The number of small cylinders in the microscopic model was set to $0 \leq N_r \leq 3$ and $8 \leq N_\theta \leq 150$.

The variables were non-dimensionalized with D as the length scale, c_∞ as the velocity scale and ρ_∞ as the unit of density unless stated explicitly.

3. Results: microscopic model

In this section, we show the numerical results obtained for the microscopic model. Figure 3 compares the pressure field between $N_\theta = 150$, 12 and 0 for $N_r = 1$, where $N_\theta = 0$ corresponds to the bare cylinder; it shows the mean pressure $\bar{\Delta p} = \bar{p} - p_\infty$ and the fluctuation pressure defined as $\Delta p_{fluct} = p - \bar{p}$, where $\bar{p}$ is the time average of p; in the far field, the fluctuation pressure almost coincides with the sound pressure because Δp_{fluct} satisfies the basic properties of linear acoustic waves as shown in Appendix D. The contour levels are the same for all panels. The mean pressure distributions are similar, although some differences are observed in the wake. In figures 3(*b*) and 3(*f*), we observe that the acoustic waves propagate cylindrically from the origin for $N_\theta = 150$ and 0; the wavelength is larger for $N_\theta = 150$ than for $N_\theta = 0$ because the effective diameter of the cylinder is $1.8D$ for $N_\theta = 150$, while it is D for $N_\theta = 0$. However, the acoustic waves are nearly invisible for $N_\theta = 12$ (figure 3*d*). This figure shows that the sound is significantly reduced for $N_\theta = 12$.

Figure 4 shows the time evolutions of pressure measured at $(r, \theta) = (80, 90^\circ)$, the drag F_x and the lift F_y for the three cases as in figure 3. The drag and lift are calculated as the reaction force of the rate of change of momentum owing to the penalization terms:

$$\begin{aligned} F_i &= -\int_S f_i \,\mathrm{d}A \\ &= -\int_{\partial S} (\rho u_i u_j + p\delta_{ij} - \tau_{ij}) n_j \,\mathrm{d}l - \frac{\mathrm{d}}{\mathrm{d}t}\int_S \rho u_i \,\mathrm{d}A, \end{aligned} \tag{3.1}$$

where $\boldsymbol{f}$ is the force per unit area owing to the penalization terms, S is any region including the cylinder and the porous material, and $\boldsymbol{n}$ is the unit outward normal vector on S. In the

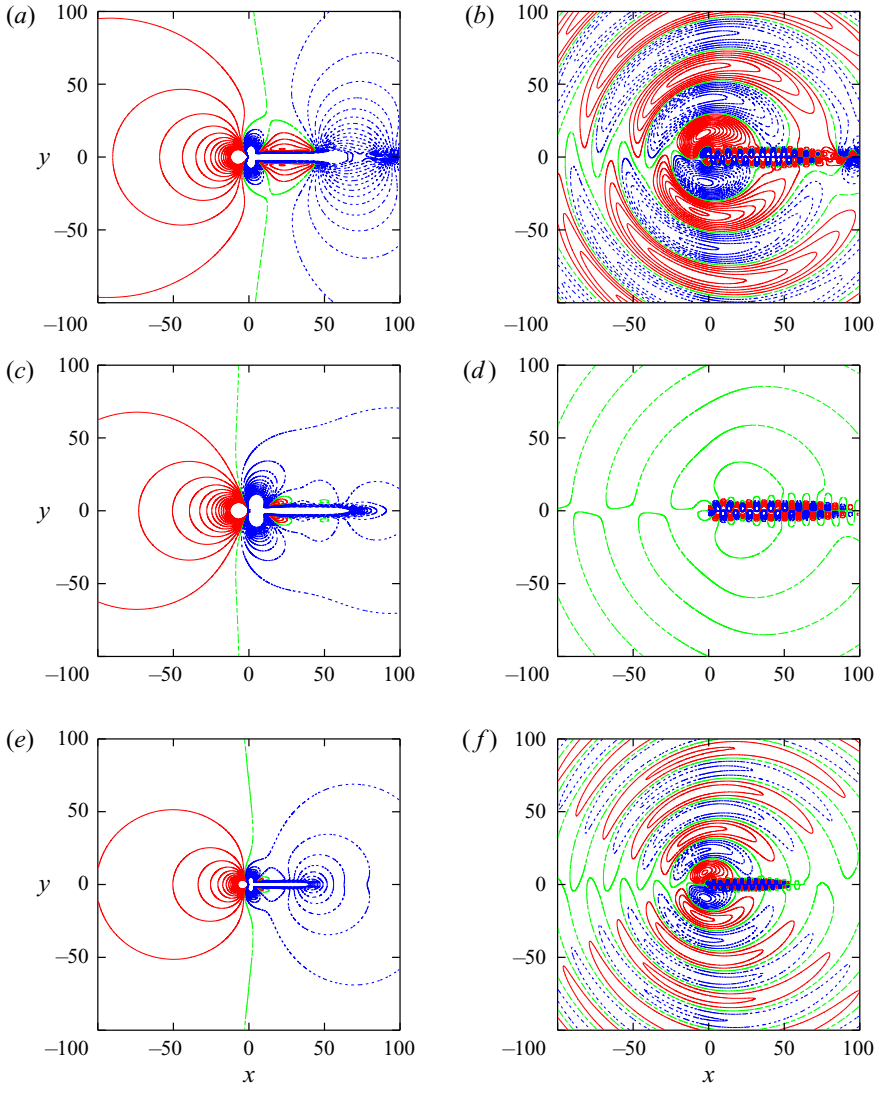

Figure 3. Pressure field shown by contour lines of mean pressure $\overline{\Delta p} = \bar{p} - p_\infty$ (*a*,*c*,*e*) and fluctuation pressure $\Delta p_{fluct} = p - \bar{p}$ at $t = 1100$ (*b*,*d*,*f*). Microscopic model with $N_r = 1$. Red lines, $\Delta p > 0$; green lines, $\Delta p = 0$; blue lines, $\Delta p < 0$. The contour levels are $|\Delta p| \leq 8.0 \times 10^{-4}$ with the increment $\Delta p_{inc} = 5.0 \times 10^{-5}$. (*a*,*b*) $N_\theta = 150$, (*c*,*d*) $N_\theta = 12$, (*e*,*f*) $N_\theta = 0$.

following, the region S is set to the rectangle $[-3D, 12D] \times [-3D, 3D]$ after confirming that the results do not depend on the choice of the region. Nearly sinusoidal oscillations of the pressure are observed for $N_r = 150$ and 0, while the amplitude and the time period for $N_r = 150$ are larger than those for $N_r = 0$. However, the fluctuation pressure is small for $N_r = 12$, as observed in figure 3(*b*). The aeroacoustic sound in the present problem is dominated by the time variation of the lift (figure 4*c*) rather than that of the drag (figure 4*b*) in the framework of acoustic analogies: we can observe that the amplitude of the lift oscillations is larger for $N_r = 150$ than $N_r = 0$; it almost vanishes for $N_r = 12$; and the time periods of the lift oscillations are the same as those of the fluctuation pressure.

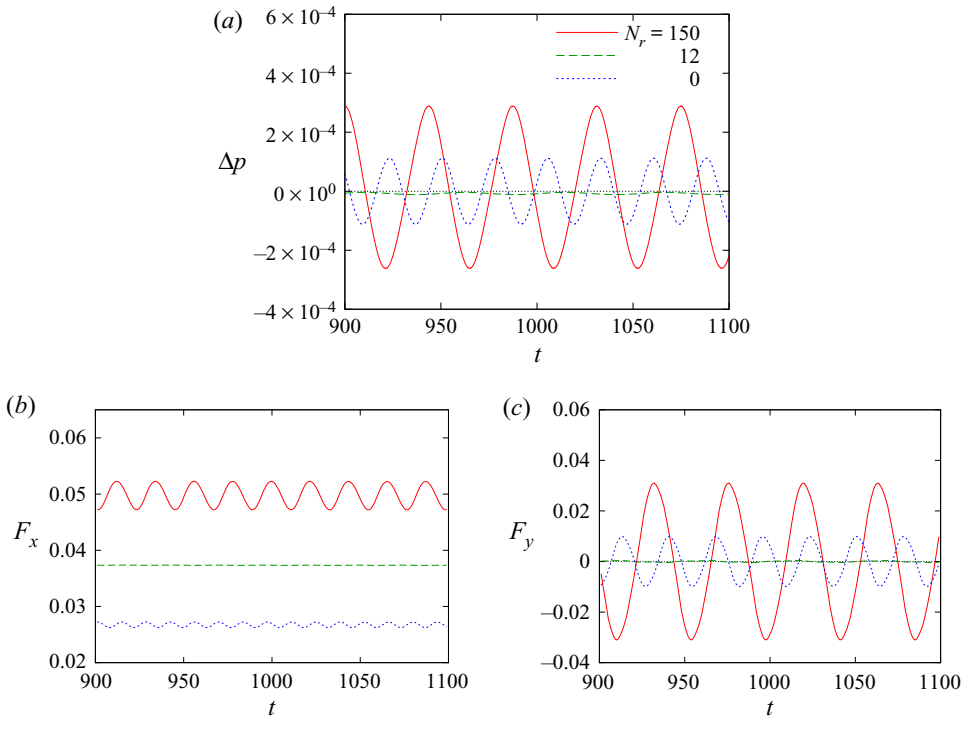

Figure 4. Time evolution of pressure at $(r, \theta) = (80, 90^\circ)$ (*a*), drag F_x (*b*) and lift F_y (*c*). Microscopic model with $N_r = 1$. Comparison between $N_\theta = 150$, 12 and 0.

We will show how the mean drag and the root-mean-square (r.m.s.) amplitude of lift depend on the number of small cylinders later in this section.

Figure 5 compares the directivity of the sound between $N_\theta = 150$, 12 and 0 for $N_r = 1$; the r.m.s. amplitudes of the acoustic waves are shown by a polar plot. It shows that the sound for $N_\theta = 150$ and 0 is dominated by a dipolar component with maximum at $\theta \approx \pm 90^\circ$, as is well known for the aeolian tone. However, the directivity for $N_\theta = 12$, which is magnified in figure 5(*b*), is not of dipolar nature. It shows that the sound arising from vortex shedding is suppressed nearly completely.

In figure 6, the acoustic power is plotted against the number N_θ of small cylinders in the azimuthal direction. It is calculated at $r = 80$ as

$$P = \int_0^{2\pi} \frac{(\Delta p_{fluct})^2}{\rho_\infty c_\infty} r \, \mathrm{d}\theta, \tag{3.2}$$

while 23 observation points at $\theta = 15^\circ, 30^\circ, \ldots, 345^\circ$ are used to discretize the above integral; $\theta = 0^\circ$ is excluded because the fluctuation pressure is dominated by hydrodynamic pressure owing to vortices in the wake and the acoustic pressure of the dipolar sound is small. The acoustic power does not change very much for $N_\theta \geq 100$; it is approximately five times larger than that for the bare cylinder $N_\theta = 0$. For $N_r = 1$, the acoustic power decreases as N_θ decreases for $N_\theta \geq 15$. The minimum at $N_\theta = 12$ is $P = 5.90 \times 10^{-9}$, which is 0.36 % (24.4 dB reduction) of the bare cylinder and 0.064 % (32.0 dB reduction) of $N_\theta = 150$, showing a significant reduction of the acoustic power. The reduction effects are weaker for $N_r = 2$ and 3 as the minimum acoustic power is 25 %

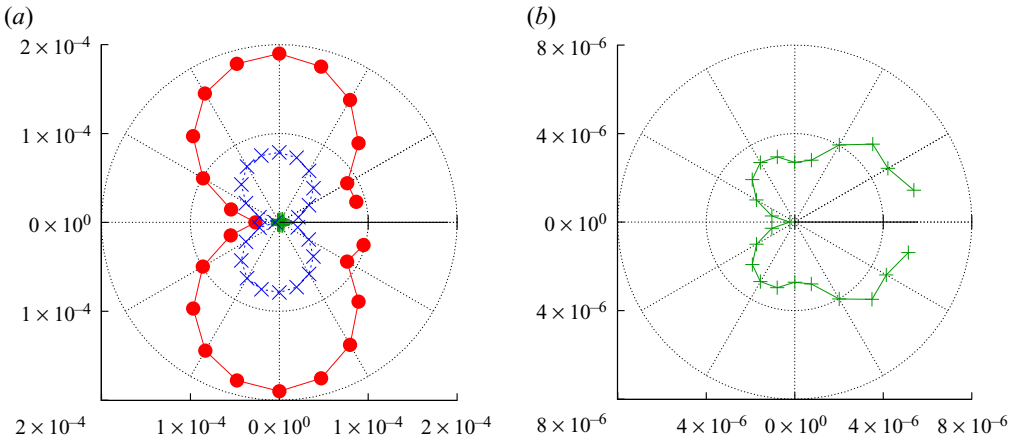

Figure 5. Directivity of r.m.s. amplitude of pressure fluctuations shown by a polar plot. Microscopic model with $N_r = 1$. (*a*) Comparison between $N_\theta = 150$ (• - red), $N_\theta = 12$ (+ - green) and $N_\theta = 0$ (× - blue); (*b*) magnified plot of $N_\theta = 12$.

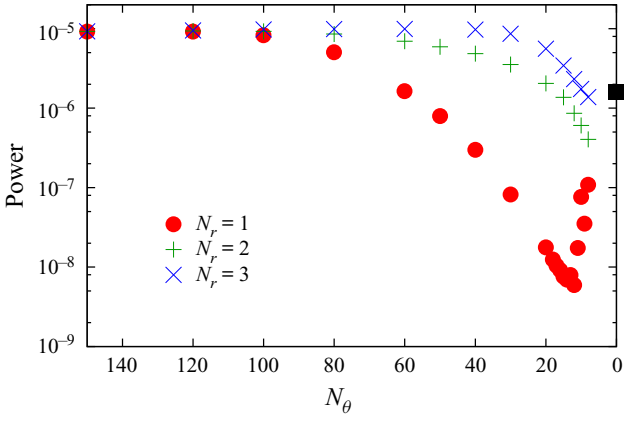

Figure 6. Acoustic power plotted against N_θ. Microscopic model: • - red, $N_r = 1$; + - green, $N_r = 2$; × - blue, $N_r = 3$; ■ - black, bare cylinder.

(6.0 dB reduction) and 85 % (0.7 dB reduction) of the bare cylinder for $N_r = 2$ and 3, respectively.

Figure 7 shows contours of vorticity for $N_\theta = 150$, 12 and 0 with $N_r = 1$. Two instants of opposite phase, one of which is the final time of simulation $t = 1100$, are shown for each case as the vortex motion is periodic; note that the other instant depends on the case because the time period is different between the three cases. For $N_\theta = 150$ and 0, vortex shedding behind the cylinder is observed. For $N_\theta = 12$, however, vortices are not shed just behind the cylinder; it is delayed to $x \approx 12$; a nearly steady wake is formed for $0 \leq x \lesssim 12$. The flow is blocked by the small cylinders so that a thick boundary layer is formed around the bare cylinder. As a result, the wake is stabilized, for which the details are discussed in § 6. In figure 8, the mean flow and the fluctuation of the streamwise velocity are shown at several positions in the wake. It shows that the mean flow does not change behind the cylinder for $N_\theta = 12$, while the width of the wake quickly broadens for $N_\theta = 150$. It also confirms that the fluctuation is small for $N_\theta = 12$. It is interesting to see that the mean

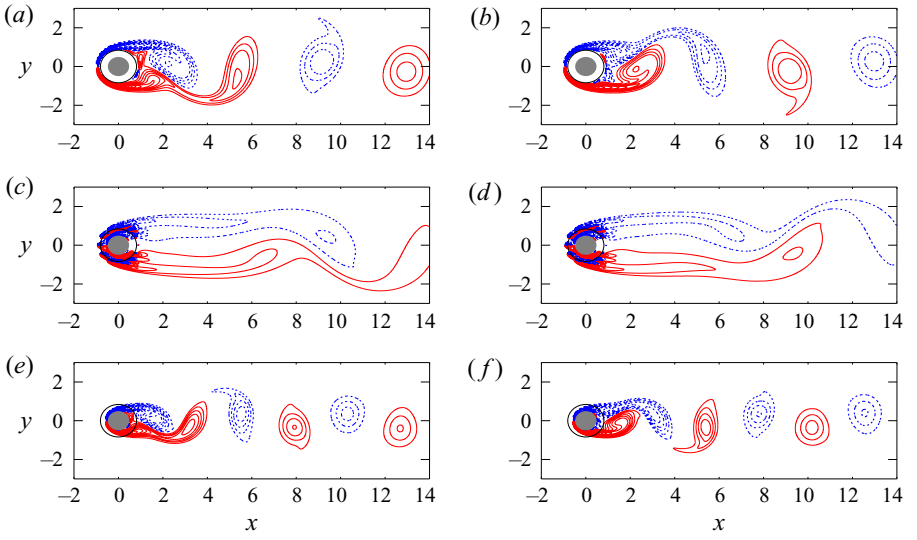

Figure 7. Vorticity field shown by contour lines. Microscopic model with $N_r = 1$: red lines, $\omega > 0$; blue lines, $\omega < 0$. The contour levels are $|\omega| \leq 2.0$ with the increment $\Delta\omega = 0.1$. The core cylinder is shown by the filled grey circles, while the outer boundary of the porous material is marked by the black circles. (*a*) $N_\theta = 150$, $t = 1078$, (*b*) $N_\theta = 150$, $t = 1100$, (*c*) $N_\theta = 12$, $t = 1074$, (*d*) $N_\theta = 12$, $t = 1100$, (*e*) $N_\theta = 0$, $t = 1087$, (*f*) $N_\theta = 0$, $t = 1100$.

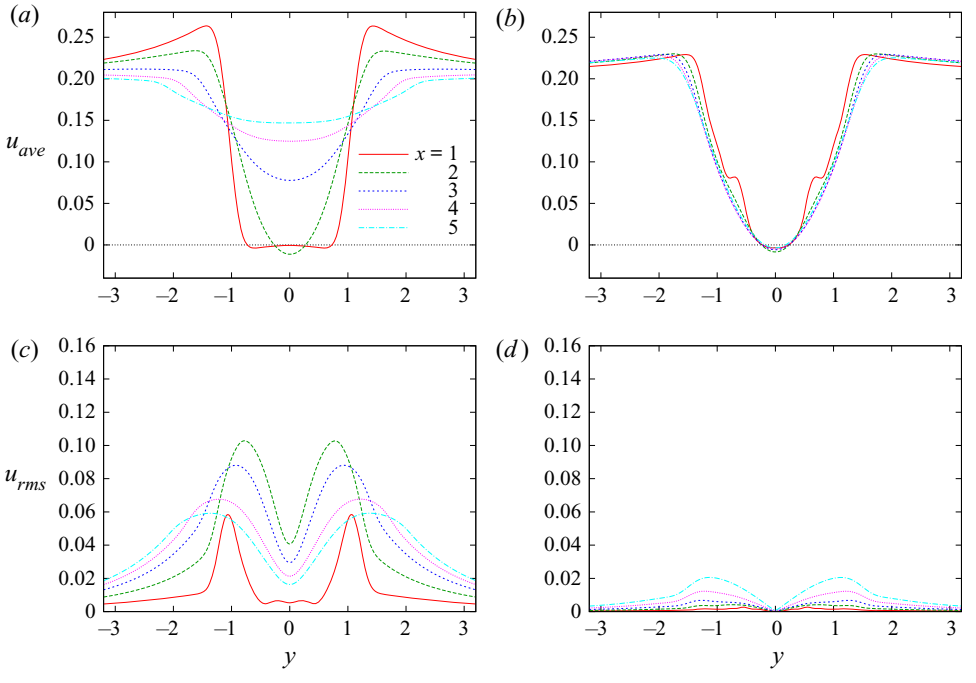

Figure 8. (*a*,*b*) Averaged wake velocity distribution and (*c*,*d*) r.m.s. amplitude of wake velocity fluctuation. Microscopic model with $N_r = 1$. (*a*,*c*) $N_\theta = 150$, (*b*,*d*) $N_\theta = 12$.

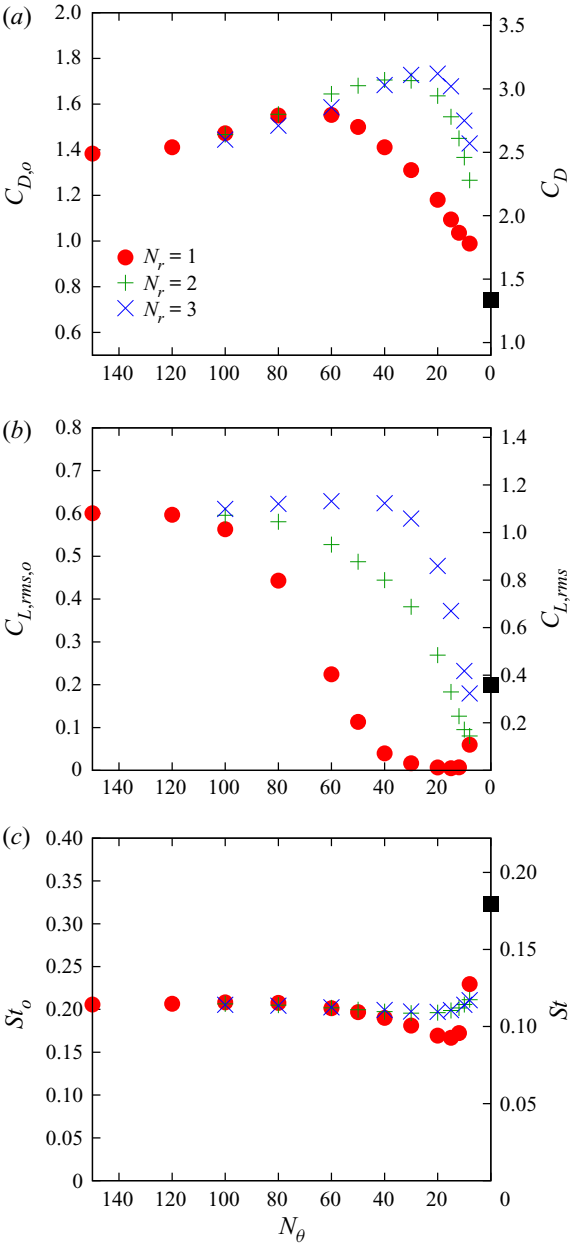

Figure 9. (*a*) Mean drag coefficient, (*b*) r.m.s. amplitude of lift coefficient and (*c*) Strouhal number plotted against N_θ. Microscopic model: • - red, $N_r = 1$; + - green, $N_r = 2$; × - blue, $N_r = 3$; *square* - black, bare cylinder.

flow and the fluctuation shown in figure 8 are similar to those observed in the experiment (Sueki *et al.* 2010) at $Re = 4.6 \times 10^4$ shown in figures 10 and 11 of Sueki *et al.* (2010) in spite of the large difference in the Reynolds number.

It is of interest to check how the drag and lift vary with the number of the small cylinders. Figure 9 shows the mean drag coefficient, the r.m.s. amplitude of the lift coefficient and the Strouhal number plotted against N_θ for $N_r = 1$, 2 and 3. They are non-dimensionalized

using the outer diameter D_o in the left vertical axis, which is suitable for large N_θ, and the inner diameter D in the right vertical axis, which is suitable for small N_θ as

$$C_{D,O} = \frac{\overline{F_x}}{(1/2)\rho_\infty U_\infty^2 D_o}, \quad C_{L,rms,O} = \frac{\sqrt{\overline{F_y^2}}}{(1/2)\rho_\infty U_\infty^2 D_o}, \quad St_O = \frac{D_o}{U_\infty T_p}, \tag{3.3}$$

$$C_D = \frac{\overline{F_x}}{(1/2)\rho_\infty U_\infty^2 D}, \quad C_{L,rms} = \frac{\sqrt{\overline{F_y^2}}}{(1/2)\rho_\infty U_\infty^2 D}, \quad St = \frac{D}{U_\infty T_p}, \tag{3.4}$$

where T_p is the time period of fluid motion. The drag coefficient and the r.m.s. lift coefficient for the bare cylinder are $C_D = 1.337$ and $C_{L,rms} = 0.350$, which are close to the values 1.368 and 0.383 obtained by Ali *et al.* (2013) and our previous results 1.332 and 0.364 in the body-fitted coordinate system and 1.300 and 0.350 by the volume penalization method (Komatsu *et al.* 2016); for $(N_r, N_\theta) = (3150)$ approximately corresponding to the large cylinder of diameter D_o and $Re = 270$, they are $C_{D,O} = 1.379$ and $C_{L,rms,O} = 0.599$, which are in reasonable agreement with $C_{D,O} = 1.358$ and $C_{L,rms,O} = 0.559$ obtained by interpolation using the coefficients at $Re = 250$ and 300 obtained by Rajani, Kandasamy & Majumdar (2009). The value of the drag for $N_\theta = 150$ coincides with that of the bare cylinder of diameter $1.8D$, which is shown later in figure 14. The drag for $N_\theta > 0$ is larger than that of the bare cylinder in the entire range. There is a range of N_θ in which the drag exceeds the value at $N_\theta = 150$: $N_\theta \geq 40$ for $N_r = 1$, $N_\theta \geq 12$ for $N_r = 2$ and $N_\theta \geq 8$ for $N_r = 3$. The maximum drag coefficient is $C_{D,O} = 1.733$ or $C_D = 3.120$ for $(N_\theta, N_r) = (20, 3)$, which is 2.3 times the drag of the bare cylinder. In these ranges, the distance between the small cylinders is large enough to allow the incoming flow to form a wake behind them; as a result, the drag exerted on each small cylinder becomes large. It is pointed out that the drag coefficient for $(N_\theta, N_r) = (12, 1)$, for which the acoustic power is minimum, is $C_{D,O} = 1.036$ or $C_D = 1.865$, which is 40 % larger than the drag of the bare cylinder. However, the r.m.s. amplitude of lift coefficient does not increase very much as N_θ decreases from $N_\theta = 150$. It decreases and nearly vanishes to $C_{L,rms,O} < 0.0072$ or $C_{L,rms,O} < 0.013$ for $12 \leq N_\theta \leq 20$ at $N_r = 1$, which corresponds to the significant reduction of the acoustic power. The Strouhal number does not change significantly for $N_\theta \gtrsim 30$, which shows that the effective radius of the porous cylinder is the outer diameter D_O; it increases with decreasing N_θ for $N_\theta \lesssim 15$ as the effective radius shifts gradually to that of the inner diameter D.

4. Results: macroscopic model

In this section, we show the results obtained for the macroscopic model. Figure 10 compares the fluctuation pressure field between three values of permeability: $\eta = 10^{-3}$, at which the porous material can be regarded as a rigid body; $\eta = 10$, at which the acoustic power is minimum; and $\eta = 10^3$, at which the porous material can be ignored (the case of the bare cylinder). This figure is similar to figure 3 showing the fluctuation pressure field for the microscopic model. In fact, figure 3(*a*) and figure 10(*a*) correspond to the case of the large cylinder of diameter $1.8D$, while figure 3(*c*) and figure 10(*c*) correspond to the case of the bare cylinder. However, there is a difference between the states of the minimum acoustic power: although the amplitude of the fluctuation pressure at $\eta = 10$ is small, weak acoustic waves propagating cylindrically can be recognized in figure 10(*b*) as the amplitude of the sound is larger than that in figure 3(*b*).

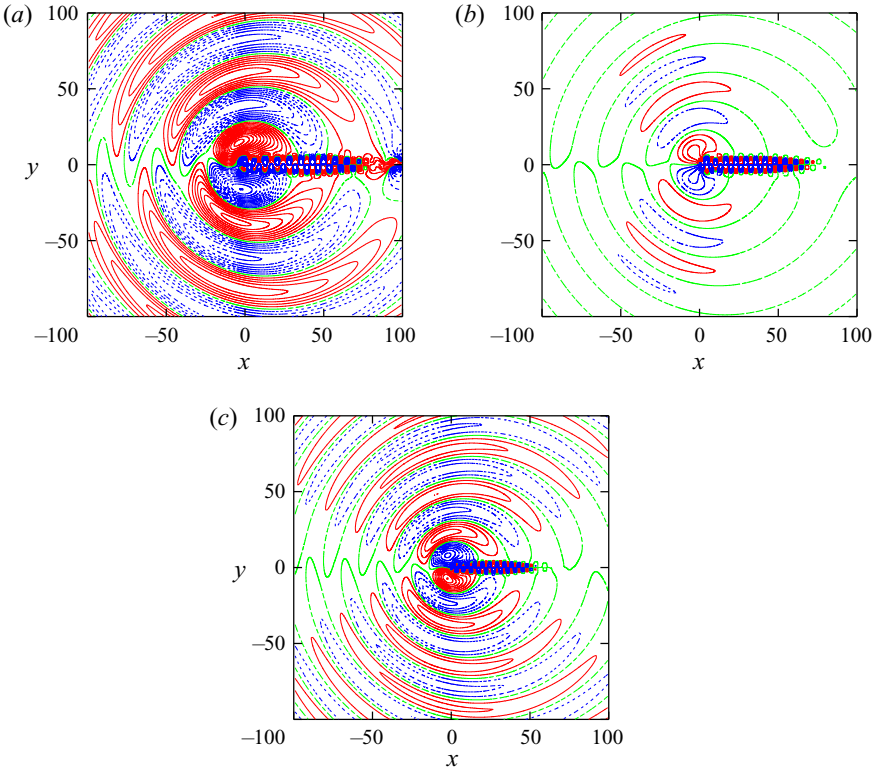

Figure 10. Pressure field shown by contour lines of fluctuation pressure $\Delta p_{fluct} = p - \bar{p}$ at $t = 1100$. Macroscopic model. The line colours and the contour levels are the same as in figure 3. (*a*) $\eta = 10^{-3}$, (*b*) $\eta = 10$, (*c*) $\eta = 10^{3}$.

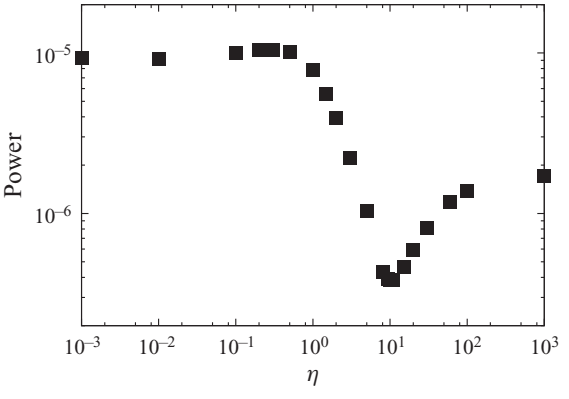

Figure 11. Acoustic power plotted against permeability η. Macroscopic model.

Figure 11 shows the acoustic power P plotted against permeability η. The values of P at $\eta = 10^{-3}$ and 10^{3} coincide with those at $N_\theta = 150$ and 0 for the microscopic model, respectively. The acoustic power increases slightly as η increases from $\eta = 10^{-3}$. It decreases for $0.2 < \eta < 10$ taking the minimum at $\eta = 10$. The acoustic power increases monotonically with η for $\eta > 10$. The minimum value at $\eta = 10$ is $P = 3.85 \times 10^{-7}$, which is 4.1 % (13.8 dB reduction) of $\eta = 10^{-3}$ and 22 % (6.5 dB reduction) of the

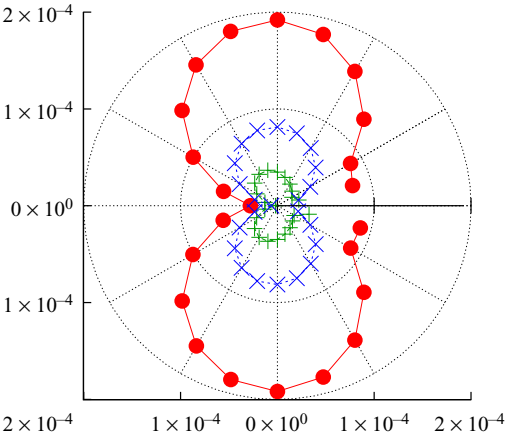

Figure 12. Directivity of r.m.s. amplitude of pressure fluctuations shown by a polar plot. Macroscopic model. Comparison between $\eta = 10^{-3}$ (• - red), $\eta = 10$ (+ - green) and $\eta = 10^3$ (× - blue).

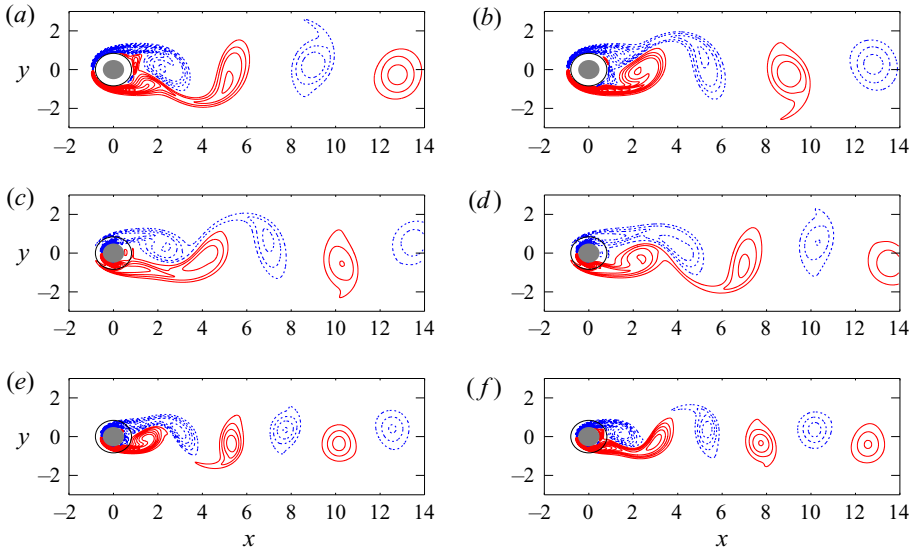

Figure 13. Vorticity field shown by contour lines. Macroscopic model. The line colours, contour levels and the cylinders are the same as in figure 7. (*a*) $\eta = 10^{-3}$, $t = 1078$, (*b*) $\eta = 10^{-3}$, $t = 1100$, (*c*) $\eta = 10$, $t = 1081$, (*d*) $\eta = 10$, $t = 1100$, (*e*) $\eta = 10^3$, $t = 1086$, (*f*) $\eta = 10^3$, $t = 1100$.

bare cylinder. This value of P is much larger than the minimum obtained for the microscopic model. This point will be examined in the next section.

Figure 12 shows the directivity of the sound for $\eta = 10^{-3}$, 10 and 10^3. The directivity nearly coincides with that of the microscopic model (figure 5) for $\eta = 10^{-3}$ and 10^3. However, the directivity at $\eta = 10$ is also dominated by the dipolar component in contrast to that of $N_\theta = 12$ in figure 5. This is understood by the flow field behind the cylinder. Figure 13 compares the vorticity field in the wake of the cylinder between the three values of η. The boundary layer on the cylinder surface is thicker for $\eta = 10$ than for $\eta = 10^{-3}$ and 10^3 as in the case of $N_\theta = 12$ in the microscopic model (figure 7*b*). However, the vortex shedding is only slightly delayed in comparison to the case of the

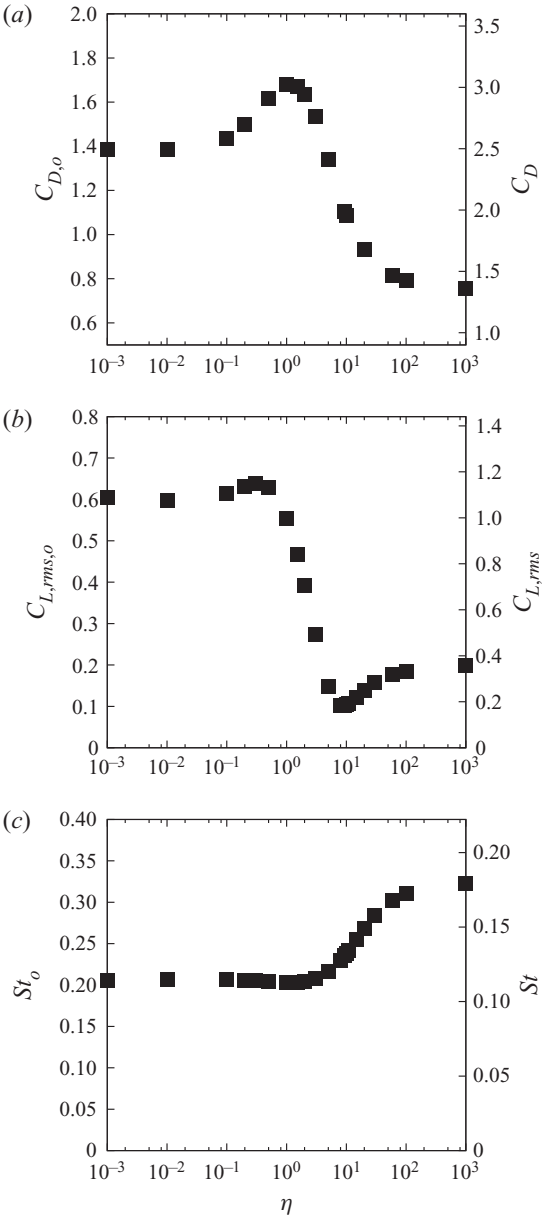

Figure 14. Mean drag coefficient, r.m.s. amplitude of lift coefficient and Strouhal number plotted against permeability η. Macroscopic model.

microscopic model. The size of the vortices and the frequency of vortex shedding are close to those for the large cylinder ($\eta = 10^{-3}$). However, the effective radius of the cylinder is close to that of the bare cylinder ($\eta = 10^{3}$). These combined effects make the acoustic power small, although the reduction rate is smaller than the microscopic model. Figure 14 shows the mean drag coefficient, the r.m.s. amplitude of the lift coefficient and the Strouhal number plotted against the permeability. The drag at $\eta = 10^{-3}$ coincides with that of the large cylinder. The drag increases with the permeability for $10^{-3} < \eta < 1$. Then

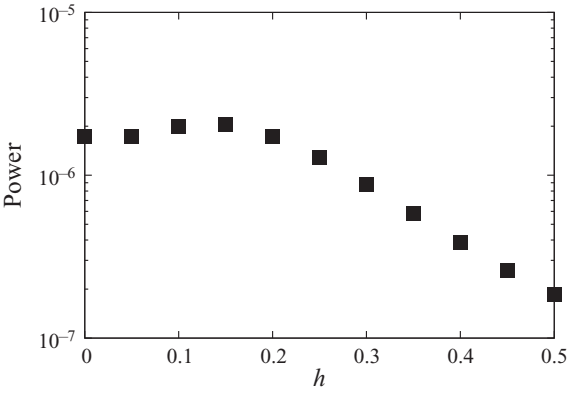

Figure 15. Minimum acoustic power plotted against thickness h of porous material.

it decreases monotonically for $1 < \eta < 10^3$, reaching the value for the bare cylinder at $\eta = 10^3$. The drag coefficient at the minimum acoustic power (at $\eta = 10$) is $C_{D,O} = 1.086$ or $C_D = 1.955$, which is 44 % larger than that of the bare cylinder. The amplitude of the lift coefficient takes a minimum at $\eta \approx 10$ for which the acoustic power is minimum; however, the minimum of $C_{L,rms}$ is $C_{L,rms,O} = 0.102$ or $C_{L,rms} = 0.184$ which is much larger than that in the microscopic model. The Strouhal number increases smoothly for $1 \lesssim \eta \leq 10^3$, which suggests that the effective radius of the porous cylinder decreases from D_O to D.

Figure 15 shows the effects of the thickness of the porous material on the minimum acoustic power. The minimum acoustic power is slightly larger than that of the bare cylinder for $0 < h < 0.2D$. However, it decreases with the thickness for $0.15D < h < 0.5D$. It is of some interest to optimize the thickness for sound reduction; however, it is postponed for a future work because prior to this, we should find the relation between the microscopic and macroscopic models.

5. Relation between microscopic and macroscopic models

In § 4 we showed that the minimum of the acoustic power obtained for the macroscopic model is much larger than that obtained for the microscopic model (§ 3). In this section, we introduce a modified macroscopic model and show that the results obtained for it are consistent with those obtained for the microscopic model. Figure 16(a) shows the microscopic model with $N_r = 1$. Because we have set the outer small cylinders at $r = 0.9D - 0.5d_s = 0.885D$, it is not appropriate to model the whole region between the small cylinders and the core cylinder as porous material when $N_r = 1$. Thus we introduce a modified model as shown in figure 16(b). In this model, there is a region occupied by a fluid between the core cylinder and the porous material of thickness h which models the small cylinders. This modified model is expected to be closer to the microscopic model with $N_r = 1$.

Figure 17 shows the acoustic power plotted against the permeability for the modified macroscopic model. The results with four values of thickness are compared: $h = 0.4D$, $0.2D$, $0.1D$ and $0.03D$. Note that $h = 0.4D$ corresponds to the original macroscopic model. As the thickness decreases, the minimum acoustic power decreases, while the value of η at the minimum also decreases. The minimum acoustic power for $h = 0.03D$ and $0.1D$ is 7.74×10^{-9} at $\eta = 0.6$ and 1.13×10^{-8} at $\eta = 2.5$, respectively, which are the same order of magnitude as that of the microscopic model.

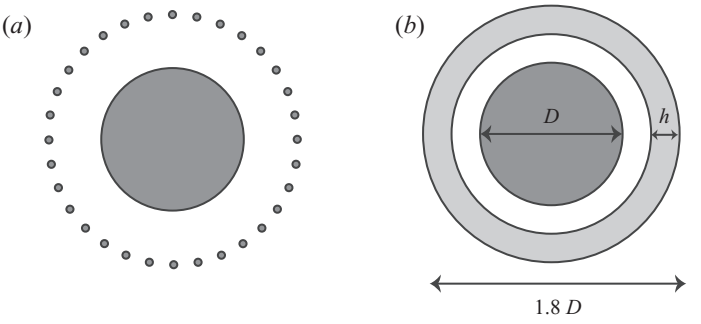

Figure 16. (*a*) Microscopic model with $N_r = 1$ and $N_\theta = 32$ and (*b*) modified macroscopic model.

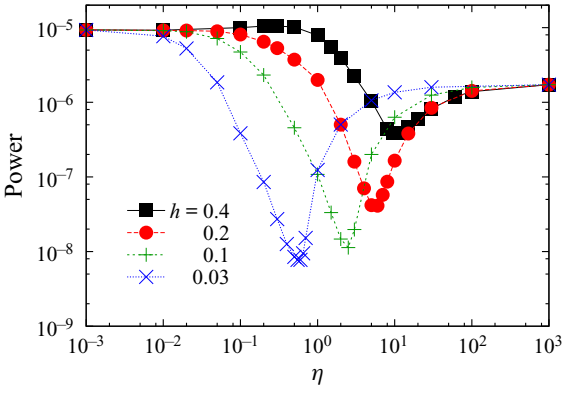

Figure 17. Acoustic power plotted against permeability η. Modified macroscopic model: *square* - black, $h = 0.4D$; • - red, $h = 0.2D$; + - green, $h = 0.1D$; × - blue, $h = 0.03D$.

Figure 18 shows the mean drag plotted against the permeability. The maximum of the mean drag decreases and shifts to smaller η as the thickness decreases. The maxima for $h = 0.03D$ and $0.1D$ are close to that of the microscopic model. The wake behind the cylinder is stabilized as observed in figure 19, which shows the vorticity field for $h = 0.03D$ at $\eta = 0.6$ and is similar to that of the microscopic model with $(N_r, N_\theta) = (12, 1)$ (figure 7*d*).

The above results for $h = 0.03D$ and $0.1D$ suggest that the modified macroscopic model is closely related to the microscopic model. To compare the results obtained with the two models, we resort to the estimate of the intrinsic permeability of fibrous media obtained by the theory of homogenization (Berdichevsky & Cai 1993; Boutin 2000; Auriault, Boutin & Geindreau 2009)

$$K_{pT} = -\frac{1}{4}\left[\log\beta + \frac{1-\beta^4}{2(1+\beta^4)}\right]R_e^2. \tag{5.1}$$

In the above equation, K_{pT} is the P estimate of the transverse intrinsic permeability, $\beta = R_s/R_e$, R_s is the radius of small cylinders modelling fibres and R_e is the external radius of a fluid shell which contains a small cylinder. The intrinsic permeability is related to the permeability η and the viscosity μ through

$$\eta = \frac{\rho_\infty c_\infty K_{pT}}{\mu D}, \tag{5.2}$$

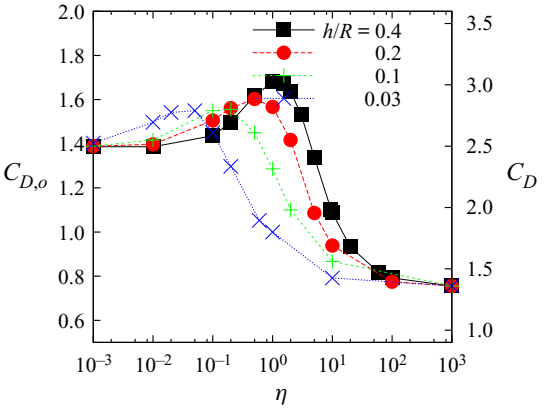

Figure 18. Drag plotted against permeability η. Modified macroscopic model: *square* - black, $h = 0.4D$; • - red, $h = 0.2D$; + - green, $h = 0.1D$; × - blue, $h = 0.03D$.

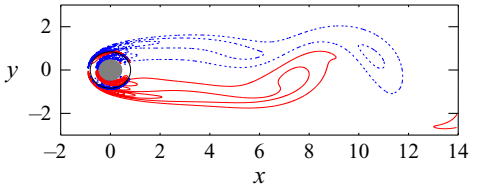

Figure 19. Vorticity field shown by contour lines. Modified macroscopic model with $h = 0.03D$ and $\eta = 0.6$. The line colours, contour levels and the cylinders are the same as in figure 7.

in the present scaling. Naturally, we can set $R_s = d_s/2$. The porosity ϕ in the above estimate is related to β by $\phi = 1 - \beta^2$, which implies that β^2 is the ratio of the area S_{cyl} occupied by the small cylinders to the area S_{por} of the porous material. In our microscopic model, we have $S_{cyl} = \pi(d_s/2)^2 N_r N_\theta$ and $S_{por} = \pi h(D_o - h)$, which allow us to express β^2 by the parameters in the microscopic model:

$$\beta^2 = 1 - \phi = \frac{S_{cyl}}{S_{por}} = \frac{d_s^2 N_r N_\theta}{4h(D_o - h)}. \tag{5.3}$$

Substituting (5.1), (5.3) and $\beta = R_s/R_e$ into (5.2), the permeability in the modified macroscopic model is expressed by the parameters in the microscopic model.

The acoustic power and the drag obtained for the microscopic model are compared with those obtained for the modified macroscopic model as a function of permeability η using the above equations in figure 20; the microscopic models with $N_r = 1$ and 3 are compared with the modified macroscopic models with $h = 0.03D$ and $0.4D$, respectively. It shows that the results obtained for the two models are in good agreement. In fact, both the acoustic power and the drag obtained for the microscopic model with $N_r = 1$ nearly collapse with those obtained for the macroscopic model with $h = 0.03D$ except for a small deviation at $\eta \gtrsim 1$, where the corresponding values of N_θ are small. The agreement between the microscopic model with $N_r = 3$ and the macroscopic model with $h = 0.4D$ looks slightly worse because variation of the acoustic power in the microscopic model occurs at small N_θ and the minimum of the acoustic power is out of the range of N_θ;

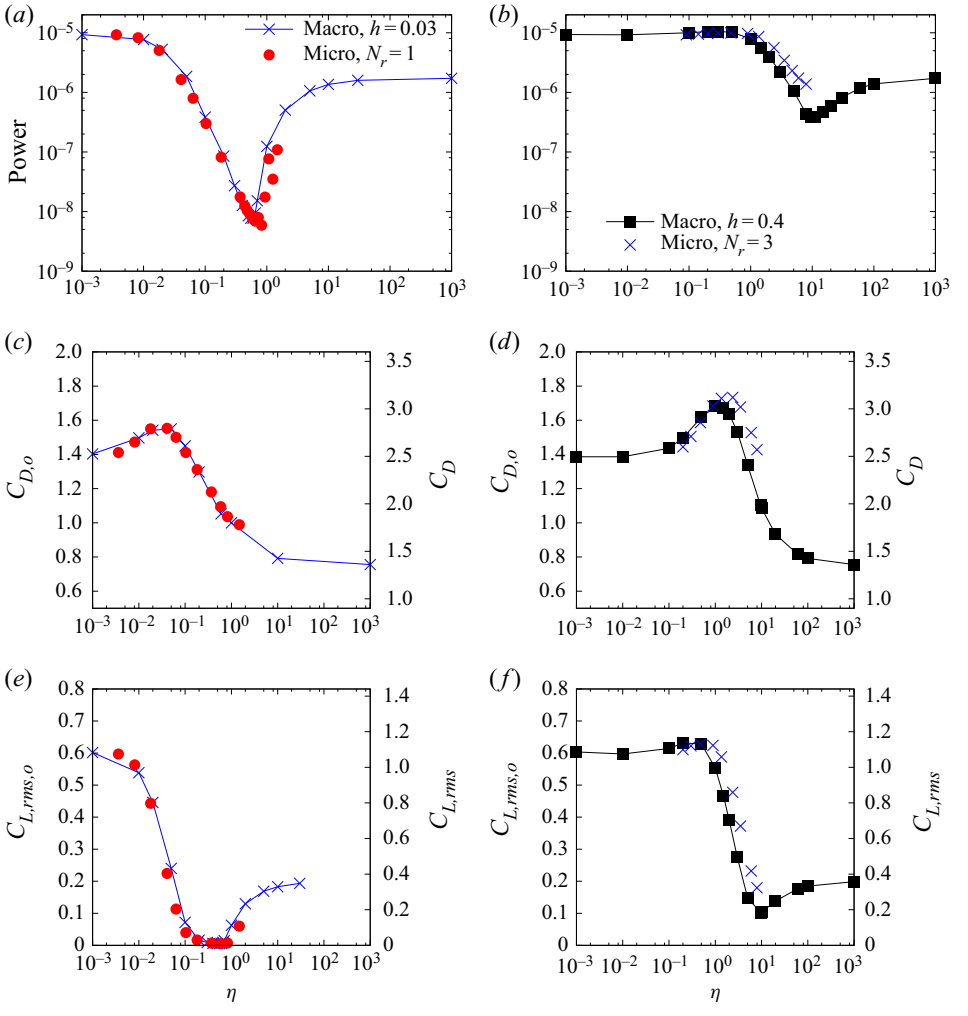

Figure 20. Comparison between modified macroscopic and microscopic models. (*a*,*b*) Acoustic power, (*c*,*d*) mean drag coefficient and (*e*,*f*) r.m.s. amplitude of lift coefficient plotted against permeability η. (*a*,*c*) × - blue, modified macroscopic model with $h = 0.03D$; • - red, microscopic model with $N_r = 1$; (*b*,*d*) *square* - black, (modified) macroscopic model with $h = 0.4D$; × - blue, microscopic model with $N_r = 3$.

however, the agreement is satisfactory as the overall trend is the same and the maxima of the drag are close.

Some discussions are required on the applicability of equations derived by homogenization in the present problem. At first sight, the small cylinders in the microscopic model are not sufficiently small or the number of them is not sufficiently large in order for the theory of homogenization to be applicable. However, the relation derived from the theory of homogenization works satisfactorily as we see above. This is because the most important assumption in homogenization holds: the Reynolds number based on the small cylinder is $Ud_s/\nu = 4.5$, which is sufficiently small; the flow around the small cylinders can be approximated by the Stokes flow. Therefore, the results support not only that the microscopic and macroscopic models are consistent but also that these two models are valid.

6. Detailed mechanism of sound reduction

In this section, we discuss the mechanism of sound reduction by the porous material in detail based on the results obtained for the modified macroscopic model.

In figure 21, we compare the time-averaged pressure and vorticity fields near the cylinder among the three cases: (i) $h = 0.03D$ and $\eta = 0.6$ at which the acoustic power is minimum in the modified macroscopic model (figure 21*a*,*b*), (ii) $h = 0.4D$ and $\eta = 10$ at which the acoustic power is minimum for $h = 0.4D$ or the original macroscopic model (figure 21*c*,*d*) and (iii) $h = 0.4D$ and $\eta = 10^{-3}$ which corresponds to the case of the large rigid cylinder of radius $0.9D$ (figure 21*e*,*f*). At $h = 0.03D$ and $\eta = 0.6$, the incoming flow splits into two parts as it attacks the porous material: a part of the incoming flow intrudes into the inside of the porous material forming a jet-like flow shown by the positive vorticity region near $r = 0.9D$ and the negative vorticity region near $r = 0.5D$; the rest of the incoming flow forms a boundary layer outside the porous material (figure 21*b*). The boundary layer outside the porous material separates at $\theta \approx 80^\circ$ to form a small separation bubble; however, it reattaches to the surface of the porous material. Alternatively, there is a flow which permeates from the inside of the porous material into its outside behind the cylinder or the wake. As a result, a thick shear layer forms in the wake (figure 21*b*). The resulting pressure field is nearly constant in the wake (figure 21*a*), which makes the wake flow nearly steady and leads to significant reduction of the aeroacoustic sound.

The acoustic power is also reduced at $h = 0.4D$ and $\eta = 10$, although the reduction rate is smaller than at $h = 0.03D$ and $\eta = 0.6$. At $h = 0.4D$ and $\eta = 10$, most portion of the incoming flow permeates into the porous material forming a thick boundary layer from the front side of the core cylinder (figure 21*d*); the boundary layer develops into a thick shear layer in the wake which is similar to that in figure 21(*b*). One notable difference is the pressure distribution in the wake: there is non-vanishing pressure gradient in the wake and the pressure on the surface of the porous material is smaller than that at $h = 0.03$ and $\eta = 0.6$ as shown by the pressure coefficient $C_p = \Delta p/((1/2)M_\infty^2$ in figure 21(*g*). As a result, the flow cannot be steady, although unsteady motion is suppressed in comparison to the case of large cylinder (figures 21*e*,*f*).

7. Concluding remarks

The effects of the porous material on the aeroacoustic sound generated in a low-Reynolds-number flow past a circular cylinder were studied by direct numerical simulation. Two models were introduced for the porous material: the microscopic model, in which the porous material is a collection of small cylinders, and the macroscopic model, in which the porous material is continuum characterized by permeability. The corrected volume penalization method (Komatsu *et al.* 2016; Hattori & Komatsu 2017) enabled us to capture aeroacoustic waves of small amplitudes as a solution to the compressible Navier–Stokes equations supplemented by penalization terms without using aeroacoustic analogies or solving additional equations. In the microscopic model, significant reduction of the aeroacoustic sound was found depending on the parameters; maximum reduction was achieved at $(N_r, N_\theta) = (1, 12)$, which gave 24.4 dB reduction in comparison to the bare cylinder. The vortex shedding behind the cylinder is delayed to the far wake to suppress the unsteady vortex motion near the cylinder, which is responsible for the aeroacoustic sound. In the macroscopic model, sound reduction was not as significant as in the microscopic model when the porous material is attached to the core cylinder; the maximum reduction in comparison to the bare cylinder is 6.5 dB. In the modified macroscopic model, however, a reduction rate comparable to the case of the microscopic

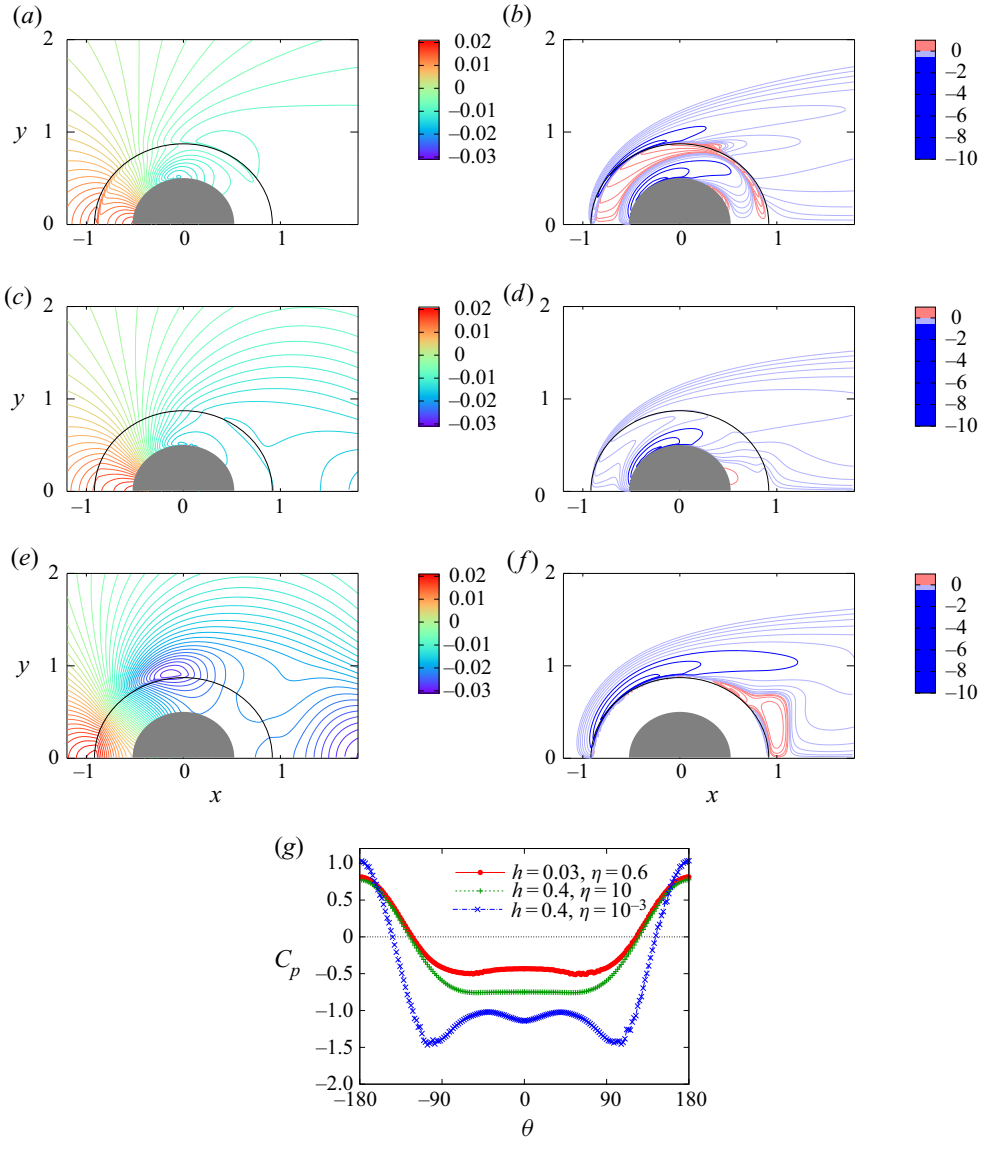

Figure 21. Comparison of mean pressure field (*a*,*c*,*e*) and mean vorticity field (*b*,*d*,*f*) near cylinder between three cases: (*a*,*b*) $h = 0.03D$ and $\eta = 0.6$ (minimum acoustic power in the modified macroscopic model), (*c*,*d*) $h = 0.4D$ and $\eta = 10$ (minimum acoustic power in the original macroscopic model) and (*e*,*f*) $h = 0.4D$ and $\eta = 10^{-3}$ (large cylinder). The core cylinder is shown by the filled grey semi-circles, while the outer boundary of the porous material is marked by the black semi-circles. In the pressure fields, time average of Δp is shown by coloured contour lines with the increment $\Delta p_{inc} = 10^{-3}$. The vorticity fields are shown by contour lines of dyadic contour levels $\omega = \pm 0.01 \times 2^n$ ($n = 0, 1, \ldots$): light blue lines, $\omega < 0$, $0 \leq n \leq 5$; blue lines, $\omega < 0$, $n \geq 6$; red lines, $\omega > 0$. Panel (*g*) compares the pressure coefficient $C_p = \Delta p/((1/2)M_\infty^2)$ on the outer boundary of the porous material ($r = 0.9D$) for the three cases.

model was found when there was a fluid region between the porous material and the core cylinder. The results obtained for the modified macroscopic model were in good agreement with those obtained for the microscopic model converted by the theory of homogenization (Berdichevsky & Cai 1993; Boutin 2000; Auriault *et al.* 2009), which established not only

that the microscopic and macroscopic models are consistent but also that these two models are valid. One of the important findings in the present study is that the reduction effect of the porous material on the aeroacoustic sound depends strongly on the properties of the porous material: it depends not only on the thickness of the porous material but also on the permeability or porosity of the porous material. For instance, the porosity should be in the range $0.91 \lesssim \phi \lesssim 0.96$ in order that the sound is reduced more than 20 dB from the bare cylinder.

It is of interest to compare the present results with the experiment by Sueki *et al.* (2010), although the Reynolds number is different. Sueki *et al.* (2010) showed the sound pressure level of the aeroacoustic noise at the vortex shedding frequency is reduced by approximately 20 dB and 30 dB in comparison to the bare cylinder and the large cylinder, respectively, while the porosity of the porous materials is larger than 97 %. The maximum reduction rate in the present study is comparable to the above values, where a 24.4 dB and 32.0 dB reduction in comparison to the bare cylinder and the large cylinder, respectively, are obtained for the microscopic model; by using the relation (5.3), the porosity at the minimum can be evaluated as $\phi = 1 - \beta^2 = 94.9\,\%$, which is smaller than the above value in the experiment. In the modified macroscopic model, however, the porous material is confined at the boundary of the large cylinder; if the region between the core and the large cylinders is regarded as the porous material, as in the original macroscopic model, the value of porosity becomes $\phi = 98.5\,\%$, which agrees with the experiment. As we have pointed out in § 3, the mean flow and the fluctuation in the wake are also similar to those observed by Sueki *et al.* (2010). Therefore, the essential mechanism of sound reduction is most likely to be the same for the present work and the experiment. This is not surprising because it is the tonal noise at the vortex shedding frequency that is significantly reduced in the study by Sueki *et al.* (2010).

However, we should further check several important differences between the present case and that of Sueki *et al.* (2010): the Reynolds number based on the small cylinder is 4.5 in the present work, which implies that the flow around the small cylinders is the Stokes flow; however, the Reynolds number based on the thickness of the small-scale structures in the porous material in the study by Sueki *et al.* (2010) is estimated as $Re = O(10^{2\sim3})$, at which vortices are shed from these structures. The flow is assumed as two-dimensional in the present case, although three-dimensional effects should be important in high-Reynolds-number flows with three-dimensional structures of the porous material in the experiment by Sueki *et al.* (2010). In the present work, the presence of the fluid region between the porous material and the core cylinder is important, while there is no such region in the experiment. One layer of small cylinders in our microscopic model is sufficient for significant reduction of the aeroacoustic sound; this is probably owing to the low Reynolds number of the flow. It is possible that the three-dimensional unsteady flow in the small structures of the porous material acts as eddy viscosity so that their overall effects are similar to the present case, which is of great interest to study as a future work. Unfortunately, it is hopeless to perform DNS based on the microscopic model for three-dimensional flows at the Reynolds numbers of the experiments because of the huge computational costs; comparison of the two models in three-dimensional moderate-Reynolds-number flows would be feasible, which is one of our future works. The present results have shown that the microscopic model can be replaced by the macroscopic model, for which the numerical costs are low, at least in the low-Reynolds-number flows; this is a starting point for validating the macroscopic model in general, although more works are required to establish the validity for higher-Reynolds-number flows.

It is well known that sound absorption and reduction of the sound speed occur in porous materials (Cervera *et al.* 2002). These effects, if present, are correctly taken into account in the microscopic model as long as the porous material is correctly modelled by the small cylinders; in the macroscopic model, they are also taken into account at least in the low-frequency or long-wave approximation under which Darcy's law is derived (Fellah & Depollier 2000) because the most important term of volume penalization in our method coincides with Darcy's law. In the present case, however, these effects are not significant because it is the pressure distribution owing to vortices and the cylinders, which is much larger than the acoustic waves near the core cylinder, that is responsible for the sound generation; in fact, the time variation of the pressure distribution arising from vortices and the cylinders produces acoustic waves under the effect of retarded time. Sound absorption and reduction of the sound speed can be important when multiple objects are placed in the flow so that the acoustic waves generated near one object reflect from other objects covered by the porous material. It would be of interest to investigate these effects together with the effects of elasticity in the porous material, which have been neglected in the microscopic model; this should be another future work.

When the two models are validated for DNS of the aeroacoustic sound in a flow involving a porous material, they can be used to optimize and design the shape and porosity of the porous material to minimize the aeroacoustic sound. In particular, numerical simulation based on the macroscopic model requires smaller costs for the parameter study than experiments as the total computational time required for the macroscopic model was 22.0 hours, while it was 58.7 hours for the microscopic model on one node (40 cores) of PRIMERGY at the Institute of Fluid Science, Tohoku University; the time increases to 738.8 hours for the microscopic model with the minimum grid spacing $\Delta x_{min}/D = 1.90 \times 10^{-3}$ used for checking numerical accuracy (Appendix B). The adjoint-based optimization can be implemented to the macroscopic model and is expected to explore new possibilities for sound reduction. Reduction of the aeroacoustic sound is an important issue in many engineering applications, as described in § 1. Although the present method focused on the effects of the porous material, it would be useful to pursue other possibilities as actual implementation of a reduction method can be prohibited by a number of reasons including cost, durability and robustness of the effects; it should be pointed out that in the present method, the drag increases and the actual size of the cylinder becomes large by using the porous material, which can be a disadvantage in some applications. In this regard, various methods proposed for suppression of vortex-induced oscillation can also be effective for reduction of the aeroacoustic sound because they reduce the fluctuation of the force exerted on the object in general (Wong & Kokkalis 1982; Blevins 1990).

Acknowledgements. Numerical calculations were performed on PRIMERGY at the Institute of Fluid Science, Tohoku University.

Declaration of interest. The authors report no conflict of interest.

Author ORCIDs.
Yuji Hattori https://orcid.org/0000-0002-1601-6416.

Appendix A. Computational grids

We adopt a rectangular grid system with non-uniform spacings because the computational domain should be large enough to capture acoustic waves in the far field and the grid spacing should be fine enough to resolve boundary layers on the rigid bodies. As performed by Komatsu *et al.* (2016), the computational domain is divided into four regions of different

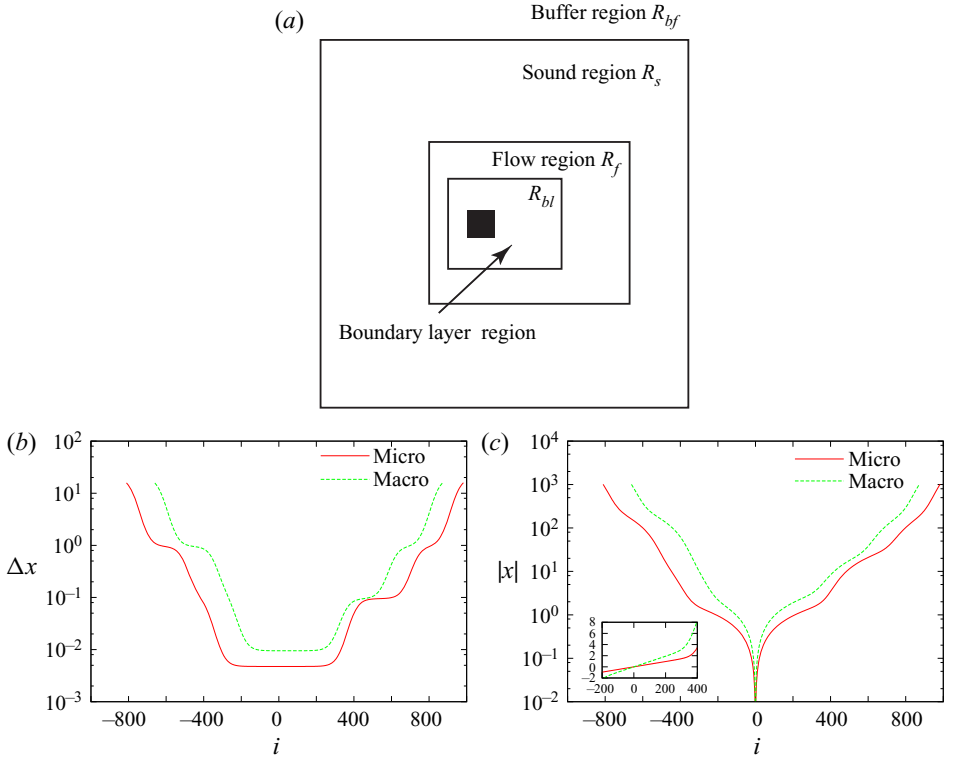

Figure 22. Computational grids: (*a*) set-up of computational grids; (*b*) grid spacing as a function of index along x axis; and (*c*) x coordinate as a function of index along x axis. In panel (*c*), the magnitude of the x coordinate is shown in log scale, while the inset shows the x coordinate near the cylinder in linear scale.

grid spacings (figure 22*a*): (i) the boundary layer region R_{bl}, in which the grid size is smaller than $0.005D$ and $0.01D$ in the microscopic and macroscopic models, respectively, (ii) the flow region R_f, in which the grid size is smaller than $0.1D$ (in both models), (iii) the sound region R_s, in which the grid size is smaller than D and (iv) the buffer region R_{bf}. The grid spacings in the first three regions are small enough to resolve boundary layers in R_{bl}, vortices in R_f and acoustic waves in R_s. In the buffer region R_{bf}, the grid spacing is prescribed to be large so that the acoustic waves are damped by the stretching of the spacing and thereby numerical reflection at the outer boundaries, which is small but does occur in spite of the non-reflecting boundary conditions, is reduced sufficiently. Table 1 lists the minimum grid size and the boundary layer and flow regions of the microscopic and macroscopic models. The sound region is larger than the square $|x|, |y| \leq 100$, while the whole region is $|x|, |y| \leq 1000$. The grid spacing is stretched smoothly, as shown in figure 22(*b*), as a function of grid index. As a result, the whole region is covered as shown in figure 22(*c*); in this figure, the magnitude of the x coordinate is shown in log scale as a function of grid index, while the inset shows the x coordinate in linear scale near the cylinder.

Appendix B. Numerical accuracy of DNS of microscopic model

It is important to check the accuracy of DNS in the microscopic model because the porous material is a collection of small cylinders of radius $d_s = 0.03$, which demands

	Δx_{min}	R_{bl}	R_f	(N_x, N_y)
Microscopic	4.75×10^{-3}	$[-1.10, 1.21] \times [-1.20, 1.20]$	$[-6.29, 21.2] \times [-6.39, 6.39]$	(1794, 1662)
Macroscopic	9.50×10^{-3}	$[-1.11, 2.12] \times [-2.06, 2.06]$	$[-5.72, 16.2] \times [-6.67, 6.67]$	(1532, 1540)

Table 1. Grid parameters. The minimum grid size and the coordinates are non-dimensionalized by D.

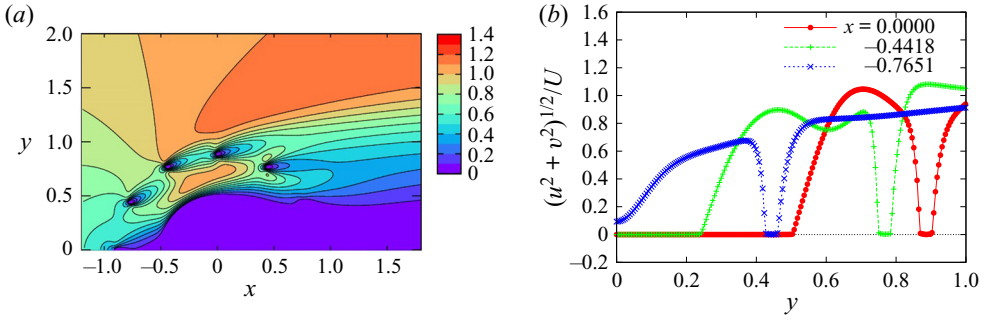

Figure 23. Distribution of magnitude of velocity $|\boldsymbol{u}|/M_\infty$. Microscopic model with $(N_r, N_\theta) = (1, 12)$. (*a*) Contours near the core cylinder; (*b*) distributions along three lines passing through small cylinders.

sufficiently high resolution. First, the no-slip boundary conditions at the small cylinders are checked in figure 23, which shows the distributions of the magnitude of velocity $|\boldsymbol{u}|/M_\infty$. In figure 23(*a*), the distribution is shown by contours. It is confirmed that the magnitude decreases quickly to zero near the small cylinders located at $(x, y) = (0, 0.885)$, $(\pm 0.443, 0.766)$ and $(-0.766, 0.443)$; the other small cylinders are not visualized because they are in the region where the magnitude is small. This supports that the no-slip boundary conditions are satisfied at the small cylinders. Figure 23(*b*) shows the distributions of $|\boldsymbol{u}|/M_\infty$ along the three lines $x = 0$, -0.4418 and -0.7651 passing through the small cylinders located at $(x, y) = (0, 0.885)$, $(-0.443, 0.766)$ and $(-0.766, 0.443)$; it is pointed out that the lines do not always pass exactly through the centres of the small cylinders; the closest grid line is chosen for each cylinder. It is observed that the velocity decreases quickly to zero at the positions of the small cylinder which are centred at $y = 0.885$, 0.766 and 0.443, with intervals of width 0.03. It is also confirmed that the boundary layers are captured with approximately seven grid points.

Figure 24 compares the time histories of pressure at $(r, \theta) = (80, 90^\circ)$ for $(N_r, N_\theta) = (3, 60)$ and $(N_r, N_\theta) = (1, 15)$ between three values of minimum grid spacings in the porous material: $\Delta x_{min}/D = 1.90 \times 10^{-3}$ (15.8 grid points in the diameter d_s), 4.75×10^{-3} (6.3 grid points) and 9.50×10^{-3} (3.2 points). They are in good agreement in each case. Although small differences are visible for $(N_r, N_\theta) = (1, 15)$, they are small in magnitude as the amplitude of the fluctuation pressure is approximately 4×10^{-6}, which is approximately 1.3 % of that for $(N_r, N_\theta) = (3, 60)$. Table 2 compares the acoustic power calculated for the two cases: P_1 for $(N_r, N_\theta) = (3, 60)$ and P_2 for $(N_r, N_\theta) = (1, 15)$. It is pointed out that the latter is close to the minimum of the acoustic power. We observe that accuracy is sufficient for the two cases; the difference in P_1 between $\Delta x_{min}/D = 1.9 \times 10^{-3}$ and 4.75×10^{-3} is 0.3 %. Although the relative errors in P_2 are higher than those in P_1 (4.4 % between $\Delta x_{min}/D = 1.9 \times 10^{-3}$ and 4.75×10^{-3}), the sound is significantly reduced in this case so that the errors are apparently amplified by

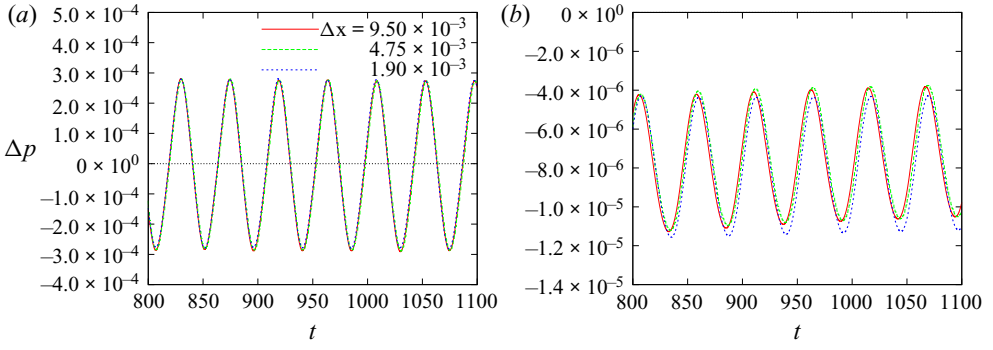

Figure 24. Dependence of time evolution of pressure at $(r, \theta) = (80, 90^\circ)$ on minimum grid size. Microscopic model: (*a*) $(N_r, N_\theta) = (3, 60)$; and (*b*) $(N_r, N_\theta) = (1, 15)$.

$\Delta x_{min}/D$	P_1	P_2
1.90×10^{-3}	9.22×10^{-6}	5.62×10^{-9}
4.75×10^{-3}	9.24×10^{-6}	5.87×10^{-9}
9.50×10^{-3}	9.29×10^{-6}	6.93×10^{-9}

Table 2. Dependence of acoustic power on minimum grid size. Microscopic model.

the small magnitude of the acoustic power. Therefore, the minimum grid size is fixed to $\Delta x_{min}/D = 4.75 \times 10^{-3}$ in the microscopic model.

Appendix C. Dependence on numerical porosity in macroscopic model

The numerical porosity ϕ_n, which appears in the penalization term in the conservation of mass (2.2), was fixed to $\phi_n = 0.98$ in the macroscopic and modified macroscopic models. It is important to check whether this choice gives correct results. It would be legitimate to impose that ϕ_n coincides with the value 0.1 for rigid bodies at $\eta = 10^{-4}$ and the penalization term vanishes ($\phi_n = 1$) at $\eta \to \infty$. One such equation is

$$\phi_n = \frac{1}{1 + 9(\eta_r/\eta)}, \quad \eta_r = 10^{-4}, \tag{C1}$$

(figure 25), while there are many other possibilities.

Figure 26 compares the acoustic power obtained with fixed numerical porosity $\phi_n = 0.98$ with that obtained by using (C 1). The two results are nearly equal (note that a few data are missing for the case using (C 1)), which shows that the results obtained with fixed numerical porosity are sufficiently accurate. It is pointed out that good agreement is observed not only for large permeability at which the difference in ϕ_n is small but also for small permeability at which the difference is large (figure 25). In fact, the value of ϕ_n does not affect the accuracy of DNS as long as the wavelength of the acoustic waves is large compared to the size of the rigid bodies (Komatsu *et al.* 2016; Hattori & Komatsu 2017).

Appendix D. Properties of fluctuation pressure

In this appendix, we show that the fluctuation pressure satisfies properties of linear acoustic waves in the far field, which confirms that it nearly coincides with the

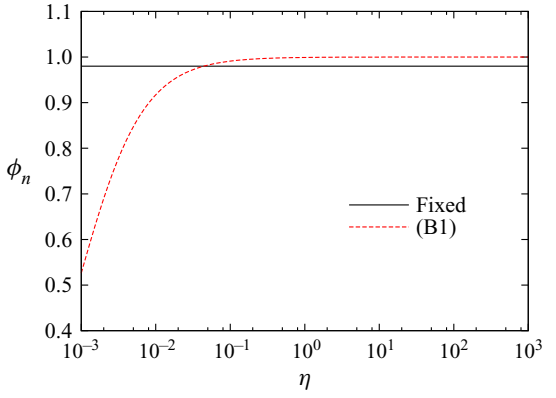

Figure 25. Relation between permeability η and numerical porosity ϕ_n of porous material in macroscopic model: black solid line, $\phi_n = 0.98$; red dashed line, (C1).

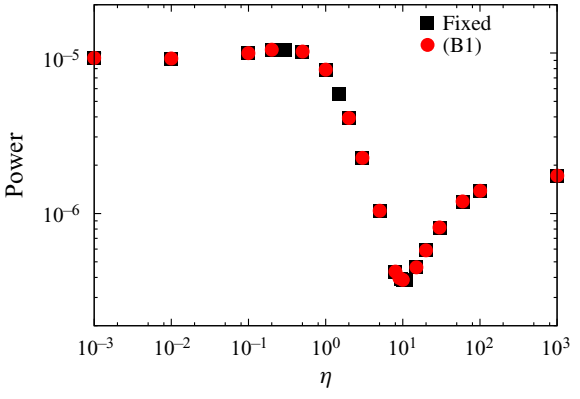

Figure 26. Acoustic power plotted against permeability η. Macroscopic model. Comparison between two different relations between numerical porosity ϕ_n and η: *square* - black, $\phi_n = 0.98$; • - red, (C1).

sound pressure. The two-dimensional linear acoustic waves are expressed in the far field as

$$p - p_\infty \approx \frac{A}{r^{1/2}} \cos\theta \sin[2\pi f(t - r/c_0) + \phi_0], \tag{D1}$$

when a dipolar sound source is oscillating sinusoidally. Figure 27 shows the dependence of the amplitude of fluctuation pressure on the distance from the origin for the microscopic model of $(N_r, N_\theta) = (3, 60)$ and $(N_r, N_\theta) = (1, 15)$; Δp_{fluct} is measured at $2.5 \leq r/D \leq 80$, while the directions $\theta = 90^\circ$ for $(N_r, N_\theta) = (3, 60)$ and $\theta = 120^\circ$ for $(N_r, N_\theta) = (1, 15)$ are close to the directions of the maximum amplitude. In both cases, the amplitude in the far field is nearly proportional to $r^{-1/2}$, which is a property of the linear acoustic waves in two dimensions; in fact, $r^{-1/2}$-dependence is observed in $r/D \gtrsim 15$ for $(N_r, N_\theta) = (3, 60)$ and in $r/D \gtrsim 40$ for $(N_r, N_\theta) = (1, 15)$; for small r, the fluctuation pressure is dominated by the hydrodynamic pressure.

Figure 28 compares the pressure $p - p_\infty$ and the fluctuation pressure Δp_{fluct} for the microscopic model of $(N_r, N_\theta) = (3, 60)$; not only the observation points in the far field but also those in the near field are considered: $r/D = 2.5$, 5, 10, 20 and 40 with $\theta = 90^\circ$. The pressure $p - p_\infty$ at $r/D = 2.5$ and 5 is negative showing that it is affected significantly

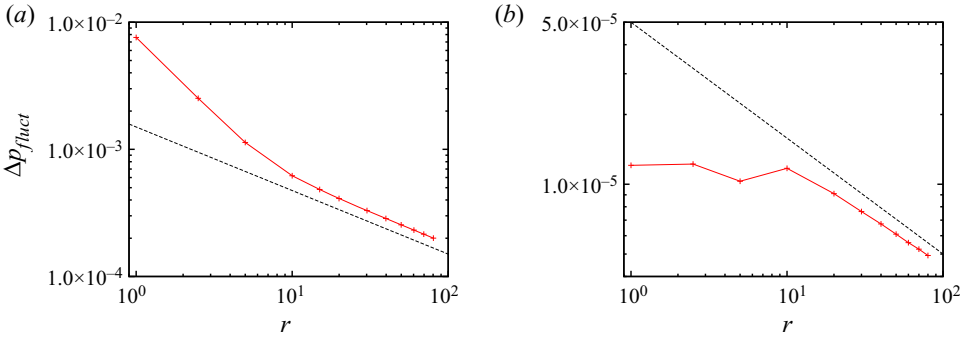

Figure 27. Amplitude of fluctuation pressure plotted against distance from origin. Microscopic model: (*a*) $(N_r, N_\theta) = (3, 60)$ and (*b*) $(N_r, N_\theta) = (1, 15)$. The observation points are $\theta = 90^\circ$ (*a*) and $\theta = 120^\circ$ (*b*) with $r/D = 2.5$, 5, 10, 20, 30, 40, 50, 60, 70 and 80. The black lines are proportional to $r^{-1/2}$.

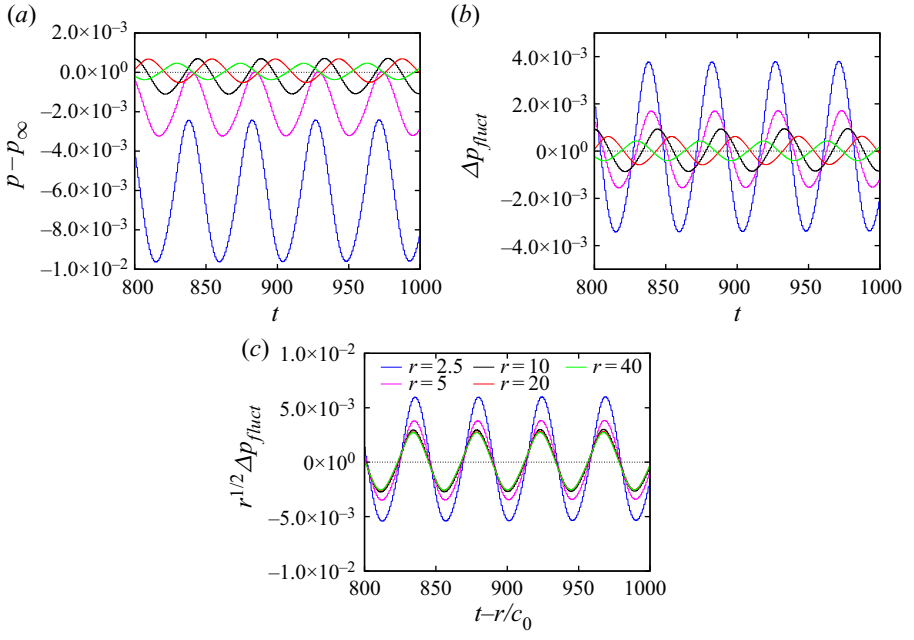

Figure 28. Comparison between pressure $p - p_0$ and fluctuation pressure Δp_{fluct}. Microscopic model with $(N_r, N_\theta) = (3, 60)$. The observation points are located at $r/D = 2.5$, 5, 10, 20 and 40 with $\theta = 90^\circ$: (*a*) $p - p_0$; (*b*) Δp_{fluct}; (*c*) Δp_{fluct} multiplied by $r^{1/2}$. In panel (*c*), the horizontal axis is replaced by the retarded time $t - r/c_0$.

by the hydrodynamic pressure which has a negative mean value. The time average of the fluctuation pressure Δp_{fluct} is zero by definition (figure 28*b*). In figure 28(*c*), the fluctuation pressure Δp_{fluct} is multiplied by $r^{1/2}$ and the retarded time $t - r/c_0$ is used as the horizontal axis. The curves for $r/D = 2.5$ and 5 are larger in amplitude than those for $r/D \geq 10$ which nearly collapse. This also confirms that the fluctuation pressure is affected significantly by the hydrodynamic pressure for $r/D = 2.5$ and 5, while in the far field $r/D \gtrsim 15$, the fluctuation pressure satisfies the property of the linear acoustic waves as further confirmed below.

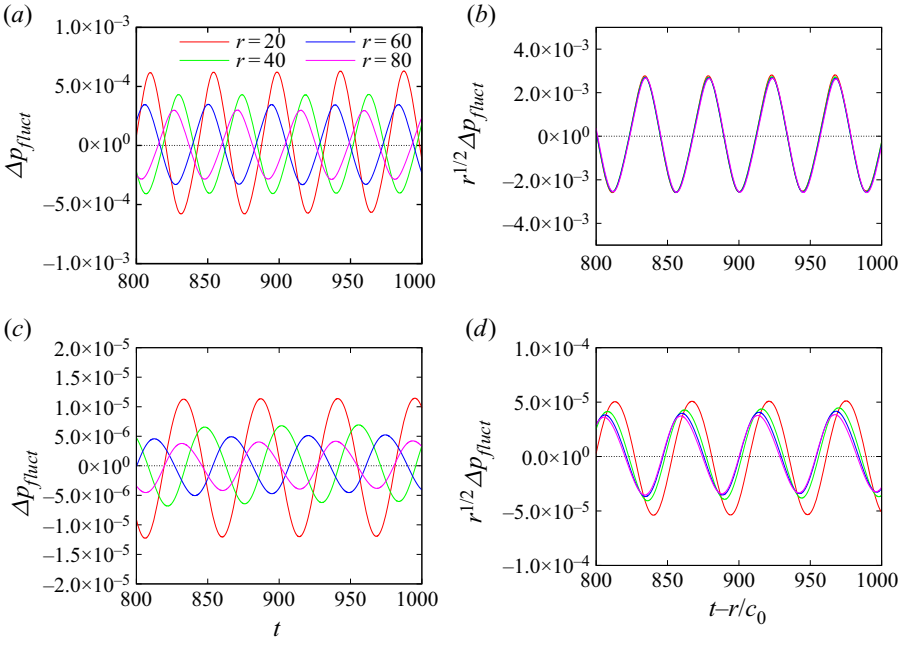

Figure 29. Time evolution of fluctuation pressure Δp_{fluct}. Microscopic model: (*a*,*b*) $(N_r, N_\theta) = (3, 60)$; and (c,d) $(N_r, N_\theta) = (1, 15)$. In panels (*a*) and (*c*), Δp_{fluct} observed at $r/D = 20, 40, 60$ and 80 with $\theta = 90^\circ$ are shown. In panels (*b*) and (*d*), the fluctuation pressure is multiplied by $r^{1/2}$ to compensate for the dependence on r, while the horizontal axis is replaced by the retarded time $t - r/c_0$.

Figure 29 shows the time evolution of the fluctuation pressure in the far field for the microscopic model of $(N_r, N_\theta) = (3, 60)$ and $(N_r, N_\theta) = (1, 15)$; Δp_{fluct} is measured at $r/D = 20, 40, 60$ and 80, while the direction is $\theta = 90^\circ$ for which the Doppler effect arising from the uniform flow vanishes. In figures 29(*a*) and 29(*c*), the amplitude and the phase of the fluctuation pressure depends on r. In figure 29(*b*), however, the curves collapse when Δp_{fluct} is multiplied by $r^{1/2}$ and the retarded time $t - r/c_0$ is used as the horizontal axis; it confirms that the fluctuation pressure nearly coincides with the sound wave propagating linearly from the origin for $r/D \geq 20$. Similar collapse except for $r/D = 20$ is also observed in figure 29(*d*), which shows that the fluctuation pressure at $r/D = 20$ is affected by pseudo sound because the sound is significantly reduced in this case. In both cases, the fluctuation pressure observed at $r/D = 80$ is sufficiently close to the sound pressure.

References

Ali, M.S.M., Zaki, S.A., Ismail, M.H., Muhamad, S. & Mahzan, M.I. 2013 Aeolian tones radiated from flow over bluff bodies. *Open Mech. J.* **7**, 48–57.

Auriault, J.-L., Boutin, C. & Geindreau, C. 2009 *Homogenization of Coupled Phenomena in Heterogeneous Media*, Chap. 10. ISTE Ltd and John Wiley & Sons Inc.

Barré, S., Bogey, C. & Bailly, C. 2008 Direct simulation of isolated elliptic vortices and of their radiated noise. *Theor. Comput. Fluid Dyn.* **22**, 65–82.

Berdichevsky, A.L. & Cai, Z. 1993 Preform permeability predictions by self-consistent method and finite element simulation. *Polym. Compos.* **14**, 132–143.

Blevins, R.D. 1990 *Flow-Induced Vibration*, Chap. 3. Van Nostrand Reinhold.

BOUTIN, C. 2000 Study of permeability by periodic and self-consistent homogenisation. *Eur. J. Mech. (A/Solids)* **19**, 603–632.

BREUGEM, W.-P., VAN DIJK, V. & DELFOS, R. 2015 Flows through real porous media: X-ray computed tomography, experiments, and numerical simulations. *Trans. ASME J. Fluids Engng* **136**, 040902.

CERVERA, F., SANCHIS, L., SÁNCHEZ-PÉREZ, J.V., MARTÍNEZ-SALA, R., RUBIO, C., MESEGUER, F., LÓPEZ, C., CABALLERO, D. & SÁNCHEZ-DEHESA, J. 2002 Refractive acoustic devices for airborne sound. *Phys. Rev. Lett.* **88**, 023902.

COLONIUS, T. & LELE, S.K. 2004 Computational aeroacoustics: progress on nonlinear problems of sound generation. *Prog. Aerosp. Sci.* **40**, 345–416.

DELFS, J., FASSMANN, B., LIPPITZ, N., LUMMER, M., MÖSSNER, M., MÜLLER, L., RURKOWSKA, K. & UPHOFF, S. 2014 SFB 880: aeroacoustic research for low noise take-off and landing. *CEAS Aeronaut. J.* **5**, 403–417.

FELLAH, Z.E.A. & DEPOLLIER, C. 2000 Transient acoustic wave propagation in rigid porous media: a time-domain approach. *J. Acoust. Soc. Am.* **107**, 683–688.

FFOWCS WILLIAMS, J.E. & HAWKINGS, D.L. 1969 Sound generation by turbulence and surfaces in arbitrary motion. *Phil. Trans. R. Soc. Lond.* A **264**, 321–342.

FREUND, J.B., LELE, S.K. & MOIN, P. 2000 Direct numerical simulation of a Mach 1.92 turbulent jet and its sound field. *AIAA J.* **38**, 3–31.

GAO, K., VAN DOMMELEN, J.A.W., GORANSSON, P. & GEERS, M.G.D. 2016 Computational homogenization of sound propagation in a deformable porous material including microscopic viscous-thermal effects. *J. Sound Vib.* **365**, 119–133.

GEYER, T. & SARRADJ, E. 2016 Circular cylinders with soft porous cover for flow noise reduction. *Exp. Fluids* **57**, 30.

GEYER, T., SARRADJ, E. & FRITZSCHE, C. 2010 Porous airfoils: noise reduction and boundary layer effects. *Intl J. Aeroacoust.* **9**, 787–820.

GIRET, J.-C. & SENGISSEN, A. 2015 Noise source analysis of a rod-airfoil configuration using unstructured large-eddy simulation. *AIAA J.* **53**, 1062–1077.

GLOERFELT, X., BAILLY, C. & JUVÉ, D. 2003 Direct computation of the noise radiated by a subsonic cavity flow and application of integral methods. *J. Sound Vib.* **266**, 119–146.

HATTORI, Y. & KOMATSU, R. 2017 Mechanism of aeroacoustic sound generation and reduction in a flow past oscillating and fixed cylinders. *J. Fluid Mech.* **832**, 241–268.

HATTORI, Y. & LLEWELLYN SMITH, S.G. 2002 Axisymmetric acoustic scattering by vortices. *J. Fluid Mech.* **473**, 275–294.

HERR, M., ROSSIGNOL, K.-S., DELFS, J., MÖSSNER, M. & LIPPITZ, N. 2014 Specification of porous materials for low noise trailing edge applications. In *20th AIAA/CEAS Aeroacoustics Conference, Atlanta, GA*, *AIAA Paper* 2014–3041.

HWANG, W.R. & ADVANI, S.G. 2010 Numerical simulations of Stokes–Brinkman equations for permeability prediction of dual scale fibrous porous media. *Phys. Fluids* **22**, 113101.

INOUE, O. & HATAKEYAMA, N. 2002 Sound generation by a two-dimensional circular cylinder in a uniform flow. *J. Fluid Mech.* **471**, 285–314.

INOUE, O. & HATTORI, Y. 1999 Sound generation by shock-vortex interactions. *J. Fluid Mech.* **380**, 81–116.

INOUE, O., HATTORI, Y. & SASAKI, T. 2000 Sound generation by coaxial collision of two vortex rings. *J. Fluid Mech.* **424**, 327–365.

IWAGAMI, S., TABATA, R., KOBAYASHI, T., HATTORI, Y. & TAKAHASHI, K. 2021 Numerical study on edge tone with compressible direct numerical simulation: sound intensity and jet motion. *Intl J. Aeroacoust.* **20**, 283–316.

KOMATSU, R., IWAKAMI, W. & HATTORI, Y. 2016 Direct numerical simulation of aeroacoustic sound by volume penalization method. *Comput. Fluids* **130**, 24–36.

LELE, S.K. 1992 Compact finite-difference schemes with spectral-like resolution. *J. Comput. Phys.* **103**, 16–42.

LIU, H., AZARPEYVAND, M., WEI, J. & QU, Z. 2015 Tandem cylinder aerodynamic sound control using porous coating. *J. Sound Vib.* **334**, 190–201.

LIU, Q. & VASILYEV, O.V. 2007 A Brinkman penalization method for compressible flows in complex geometries. *J. Comput. Phys.* **227**, 946–966.

LOPEZ PENHA, D.J., GEURTS, B.J., STOLZ, S. & NORDLUND, M. 2011 Computing the apparent permeability of an array of staggered square rods using volume-penalization. *Comput. Fluids* **51**, 157–173.

MATSUMURA, Y. & JACKSON, T.L. 2014 Numerical simulation of fluid flow through random packs of polydisperse cylinders. *Phys. Fluids* **26**, 123302.

MATSUMURA, Y., JENNE, D. & JACKSON, T.L. 2015 Numerical simulation of fluid flow through random packs of ellipses. *Phys. Fluids* **27**, 023301.

MITCHELL, B.E., LELE, S.K. & MOIN, P. 1995 Direct computation of the sound from a compressible co-rotating vortex pair. *J. Fluid Mech.* **285**, 181–202.

MITCHELL, B.E., LELE, S.K. & MOIN, P. 1999 Direct computation of the sound generated by vortex pairing in an axisymmetric jet. *J. Fluid Mech.* **383**, 113–142.

MÜLLER, B. 2008 High order numerical simulation of aeolian tones. *Comput. Fluids* **37**, 450–462.

NAITO, H. & FUKAGATA, K. 2012 Numerical simulation of flow around a circular cylinder having porous surface. *Phys. Fluids* **24**, 117102.

NAKASHIMA, Y. 2008 Sound generation by head-on and oblique collisions of two vortex rings. *Phys. Fluids* **20**, 056102.

NISHIMURA, M. & GOTO, T. 2010 Aerodynamic noise reduction by pile fabrics. *Fluid Dyn. Res.* **42**, 015003.

PERROT, C., CHEVILLOTTE, F. & PANNETON, R. 2007 Dynamic viscous permeability of an opencell aluminum foam: computations versus experiments. *J. Appl. Phys.* **103**, 024909.

POINSOT, T.J. & LELE, S.K. 1992 Boundary-conditions for direct simulations of compressible viscous flows. *J. Comput. Phys.* **101**, 104–129.

RAJANI, B.N., KANDASAMY, A. & MAJUMDAR, S. 2009 Numerical simulation of laminar flow past a circular cylinder. *Appl. Math. Model.* **33**, 1228–1247.

SUEKI, T., TAKAISHI, T., IKEDA, M. & ARAI, N. 2010 Application of porous material to reduce aerodynamic sound from bluff bodies. *Fluid Dyn. Res.* **42**, 015004.

TSUTAHARA, M., KATAOKA, T., SHIKATA, K. & TAKADA, N. 2008 New model and scheme for compressible fluids of the finite difference lattice Boltzmann method and direct simulations of aerodynamic sound. *Comput. Fluids* **37**, 79–89.

WANG, M., FREUND, J.B. & LELE, S.K. 2006 Computational prediction of flow-generated sound. *Annu. Rev. Fluid Mech.* **38**, 483–512.

WONG, H.Y. & KOKKALIS, A. 1982 A comparative study of three aerodynamic devices for suppressing vortex-induced oscillation. *J. Wind Engng Ind. Aerod.* **10**, 21–29.

XU, Y., ZHENG, Z.C. & WILSON, D.K. 2010 Simulation of turbulent wind noise reduction by porous windscreens using high-order schemes. *J. Comput. Acoust.* **18**, 321–334.